



**WAGENINGEN**  
UNIVERSITY & RESEARCH

## Rainfall-induced attenuation correction for two operational dual-polarization C-band radars in the Netherlands

Journal of Atmospheric and Oceanic Technology

Overeem, Aart; Vries, Hylke; Sakka, Hassan; Uijlenhoet, Remko; Leijnse, Hidde

<https://doi.org/10.1175/JTECH-D-20-0113.1>

This article is made publicly available in the institutional repository of Wageningen University and Research, under the terms of article 25fa of the Dutch Copyright Act, also known as the Amendment Taverne. This has been done with explicit consent by the author.

Article 25fa states that the author of a short scientific work funded either wholly or partially by Dutch public funds is entitled to make that work publicly available for no consideration following a reasonable period of time after the work was first published, provided that clear reference is made to the source of the first publication of the work.

This publication is distributed under The Association of Universities in the Netherlands (VSNU) 'Article 25fa implementation' project. In this project research outputs of researchers employed by Dutch Universities that comply with the legal requirements of Article 25fa of the Dutch Copyright Act are distributed online and free of cost or other barriers in institutional repositories. Research outputs are distributed six months after their first online publication in the original published version and with proper attribution to the source of the original publication.

You are permitted to download and use the publication for personal purposes. All rights remain with the author(s) and / or copyright owner(s) of this work. Any use of the publication or parts of it other than authorised under article 25fa of the Dutch Copyright act is prohibited. Wageningen University & Research and the author(s) of this publication shall not be held responsible or liable for any damages resulting from your (re)use of this publication.

For questions regarding the public availability of this article please contact [openscience.library@wur.nl](mailto:openscience.library@wur.nl)

## Rainfall-Induced Attenuation Correction for Two Operational Dual-Polarization C-Band Radars in the Netherlands

AART OVEREEM,<sup>a,b</sup> HYLKE DE VRIES,<sup>c</sup> HASSAN AL SAKKA,<sup>d</sup> REMKO UIJLENHOET,<sup>b,e</sup> AND HIDDE LEIJNSE<sup>a,b</sup>

<sup>a</sup> *R&D Observations and Data Technology, Royal Netherlands Meteorological Institute, De Bilt, Netherlands*

<sup>b</sup> *Hydrology and Quantitative Water Management Group, Wageningen University and Research, Wageningen, Netherlands*

<sup>c</sup> *R&D Weather and Climate Modelling, Royal Netherlands Meteorological Institute, De Bilt, Netherlands*

<sup>d</sup> *Leonardo Germany GmbH, Neuss, Germany*

<sup>e</sup> *Department of Water Management, Faculty of Civil Engineering and Geosciences, Delft University of Technology, Delft, Netherlands*

(Manuscript received 16 July 2020, in final form 22 March 2021)

**ABSTRACT:** The Royal Netherlands Meteorological Institute (KNMI) operates two operational dual-polarization C-band weather radars providing 2D radar rainfall products. Attenuation can result in severe underestimation of rainfall amounts, particularly in convective situations that are known to have high impact on society. To improve the radar-based precipitation estimates, two attenuation correction methods are evaluated and compared: 1) modified Kraemer (MK) method, i.e., Hitschfeld–Bordan where parameters of the power-law  $Z_h-k_h$  relation are adjusted such that reflectivities in the entire dataset do not exceed 59 dBZ<sub>h</sub> and attenuation correction is limited to 10 dB; and 2) using two-way path-integrated attenuation computed from the dual-polarization moment specific differential phase  $K_{dp}$  (Kdp method). In both cases the open-source Python library wradlib is employed for the actual attenuation correction. A radar voxel only contributes to the computed path-integrated attenuation if its height is below the forecasted freezing-level height from the numerical weather prediction model HARMONIE-AROME. The methods are effective in improving hourly and daily quantitative precipitation estimation (QPE), where the Kdp method performs best. The verification against rain gauge data shows that the underestimation diminishes from 55% to 37% for hourly rainfall for the Kdp method when the gauge indicates more than 10 mm of rain in that hour. The improvement for the MK method is less pronounced, with a resulting underestimation of 40%. The stability of the MK method holds a promise for application to data archives from single-polarization radars.


**KEYWORDS:** Precipitation; Radars/Radar observations; Rainfall; Remote sensing

### 1. Introduction

Operational 2D rainfall products from ground-based weather radars are extensively used for nowcasting, water management, and climatological purposes. Such products can be affected by many sources of error. For instance, a comparison of radar rainfall composites in the Netherlands against 322 manual rain gauges over 318 days, shows an average underestimation of daily rainfall of 49% (based on this study). An important source of error is severe underestimation due to rain-induced attenuation along the radar beam for X- or C-band radars (Hitschfeld and Bordan 1954; Tabary et al. 2009; Fabry 2015; Hong and Gourley 2015; Jacobi and Heistermann 2016; Zhang 2017; Rauber and Nesbitt 2018), although it can also occur for S-band radars, e.g., in a squall line (Ryzhkov and Zrníc 1995). Adjustment with gauge data can only partly compensate for underestimations and does not necessarily lead to better space–time rainfall estimates. This is particularly the case with attenuation, which is generally spatially highly variable. Moreover, the density of (sub)hourly rain gauge data is

usually low, reducing the possibilities to improve radar quantitative precipitation estimation (QPE), especially for real-time products and short time intervals. We are in the process of investigating the capabilities of our polarimetric radars to improve QPE. We do this step by step, starting with nonmeteorological echo removal (Overeem et al. 2020), followed by this study, which evaluates and compares two attenuation correction schemes applied to data from two operational radars using gauges as a reference. Hence, other possible improvements in QPE algorithms using polarimetric radars are not yet considered.

The Hitschfeld–Bordan algorithm (Hitschfeld and Bordan 1954), a single-polarization (single-pol) algorithm, estimates the two-way path-integrated attenuation (PIA) by integrating specific attenuations  $k_h$  over range, which are computed from a power-law relationship with the horizontally polarized radar reflectivity factor  $Z_h$  or rainfall intensity. This involves the use of appropriate values for the two coefficients, being representative of the rainfall type in a certain climate. The Hitschfeld–Bordan algorithm is known for problems due to growing errors, resulting in numerical instability, especially when attenuation becomes severe, e.g., exceeding 10 dB. This iterative approach can be unstable due to miscalibration of the radar as well as errors due to the assumed  $k_h$ – $Z_h$  relation (Tabary et al. 2009; Ryzhkov and Zrníc 2019). This can be remedied by employing constraints for a maximum allowed correction. Jacobi and Heistermann (2016)

 Denotes content that is immediately available upon publication as open access.

Corresponding author: Aart Overeem, [overeem@knmi.nl](mailto:overeem@knmi.nl)

DOI: 10.1175/JTECH-D-20-0113.1

© 2021 American Meteorological Society. For information regarding reuse of this content and general copyright information, consult the AMS Copyright Policy ([www.ametsoc.org/PUBSReuseLicenses](http://www.ametsoc.org/PUBSReuseLicenses)).

compare three different procedures to constrain the Hitschfeld–Bordan algorithm in Germany, where the modified Kraemer (MK) method performs best. The latter adjusts the parameters of the power-law  $k_h$ – $Z_h$  relation such that corrected reflectivities  $Z_{h,cor}$  in the entire dataset do not exceed 59 dBZ<sub>h</sub> and PIA is capped at 20 dB, where  $Z_{h,cor}$  is computed by adding PIA to  $Z_h$ .

In case of dual-polarization (dual-pol) radars, phase measurements can be employed to estimate PIA, i.e., from specific differential phase  $K_{dp}$  (Bringi et al. 1990). This involves a linear relationship between the specific attenuation and the specific differential phase:  $k_h = \gamma K_{dp}$ . The advantage of such a dual-pol method is that an independent variable can be used to estimate PIA and thus avoiding the instability issues with single-pol methods that rely on  $Z_h$  to correct  $Z_h$ . Moreover,  $K_{dp}$ , being related to signal phase rather than amplitude, is immune to (radome) attenuation, partial beam blockage, and hardware calibration errors (Hong and Gourley 2015; Rauber and Nesbitt 2018; Ryzhkov and Zrníc 2019).

This algorithm has, for instance, been applied to C-band radar data from tropical regions (Carey et al. 2000; Crisologo et al. 2014), from Mediterranean and mountainous climates in Italy (Vulpiani et al. 2012), and from X-, C- and S-band radars in France (Al-Sakka et al. 2013), though differences exist in the exact implementation. For instance, in Carey et al. (2000) the coefficient  $\gamma$  is allowed to vary along the radial and different values for the coefficient are employed in zones containing large drops and the rest of the propagation path. Another method is the rain-profiling method ZPHI, which uses the total PIA estimated from the differential phase as a constraint for a Hitschfeld–Bordan algorithm employing  $Z_h$ . For each azimuth, the total PIA is distributed based on the values of  $Z_h$  along the ray (Testud et al. 2000). Bringi et al. (2001) develop a ZPHI-based approach where the coefficient in the  $k_h$ – $K_{dp}$  relation is optimized for each time interval and ray, by minimizing differences between measured and computed profiles of differential phase. Other studies use a different value for the coefficient in strong convective cells, originally suggested by Carey et al. (2000). This involves automatic detection of these so-called hot spots and finding an optimal coefficient per ray for these cells, and using a background value for other regions. This background may be climatological or estimated from C-band radar data (Ryzhkov et al. 2007; Gu et al. 2011).

The number of studies evaluating the performance of methods to correct for rain-induced attenuation on long radar datasets from at least a few months, is limited. Usually a few to tens of case studies are evaluated. Here, we present an overview of studies involving longer radar datasets. Two groups of methods are discussed. First, considering those based on Hitschfeld–Bordan type algorithms. Van de Beek et al. (2010) apply attenuation correction to 195 events from an X-band FM-CW radar with a 15.36-km range in the Netherlands, and evaluate the improvement. Marra and Morin (2015) correct for attenuation on a 23-yr record from a C-band radar with a 150-km range in Israel, using a maximum attenuation correction of 10 dBZ, and do not specifically evaluate the attenuation correction algorithm. Thorndahl et al. (2014) apply a power-law  $k_h$ – $Z_h$  relation to correct for attenuation on a 10-yr C-band radar dataset from Denmark, up to a range of 75 km, but

specific details on the algorithm as well as a quantification of its quality are not presented. Jacobi and Heistermann (2016) apply the MK method, which outperforms other Hitschfeld–Bordan based algorithms when evaluated on a 6-yr dataset from one radar in southwest Germany. These studies do not employ hydrometeor classification, air temperatures from a numerical weather prediction model, or observations to separate liquid from solid precipitation in order to only apply attenuation correction on the former precipitation type (i.e., rain).

Second, the Kdp-based algorithms are discussed. Figueras i Ventura et al. (2012) study 29 radar-event dates for a warm period in France, where estimates within 60-km range from five C-band radars are compared with rain gauge data. Both estimates without attenuation correction and those which were corrected via a linear relation between differential phase and  $k_h$  are evaluated. Dolan et al. (2013) apply a Kdp-based attenuation correction to nearly 1100 days of radar observations for a C-band radar in Darwin, Australia, limited to 100-km range, but do not evaluate the performance of the attenuation correction. Diederich et al. (2015) evaluate 5-month datasets from two X-band radars in Germany, also quantifying the effect of an attenuation correction. Crisologo et al. (2014) apply a dual-pol algorithm employing the  $k_h$ – $K_{dp}$  relationship. That algorithm, also used in this study, is applied to a 5-month C-band radar dataset from a tropical climate (the Philippines) up to a range of 120 km, which assures that rain is the dominant precipitation type (although no hydrometeor classification or temperature information is utilized).

The lack of long-term evaluations is addressed in this study by employing a 318-day dataset from two C-band radars in the Netherlands, which is a midlatitude country ( $\sim 52^\circ\text{N}$ ,  $\sim 5^\circ\text{E}$ ) with a temperate climate. Its climatology (1990–2020) is characterized by country-average precipitation of 856 mm annually, with 220 mm in winter, 158 mm in spring, 240 mm in summer and 238 mm in autumn. Most precipitation falls as rainfall. Summer rainfall is dominated by localized convective events. A single-pol (MK method) and a dual-pol (Kdp method) based attenuation correction algorithm are evaluated and compared, which has, to the best of our knowledge, not been attempted before. This allows verification of the claim that dual-pol based attenuation algorithms can outperform single-pol based ones for operational products. The core of the attenuation correction methods is part of the open-source Python library for weather radar data processing, wradlib (Heistermann et al. 2013; Crisologo et al. 2014; Jacobi and Heistermann 2016), which facilitates reproducibility and increases the usefulness of this study. An innovation for large datasets is that in both methods forecasted freezing-level heights from the high-resolution numerical weather prediction model HARMONIE-AROME are employed (Bengtsson et al. 2017). This is done to avoid violating the assumption that all hydrometeors are raindrops. For both methods, a radar voxel only contributes to the computed PIA if its height is below this freezing-level height. Radar voxels assigned as nonmeteorological by wradlib's fuzzy echo classification algorithm (Overeem et al. 2020) do not contribute to the computation of PIA.

Relations between  $k$  on the one hand and  $Z_h$  and  $K_{dp}$  on the other are derived using measured raindrop size distributions and scattering computations. We also provide uncertainty estimates for the coefficients and exponents of these relations. These can be used to set the range of coefficients and exponents in the MK method, and to provide an uncertainty estimate of the corrected radar reflectivity factor for the Kdp method.

A systematic evaluation is performed by an extensive comparison of radar rainfall depths with gauge-based ones. This involves comparison of annual, monthly, and daily maps and verification of daily and hourly depths at 322 and 32 rain gauge locations, respectively (up to approximately 150 km to the nearest radar). The results are compared to those for which no attenuation correction has been applied. Finally, overlapping elevation scans from both radars are compared to investigate whether they match better after applying the Kdp method. Our study focuses on attenuation correction of  $Z_h$ , which is solely employed for QPE, but attenuation correction of differential reflectivity ( $Z_{dr}$ ) is not considered.

Section 2 gives a description of the employed radar, rain gauge, numerical weather prediction, and disdrometer data. In section 3 the processing chain is explained, including the removal of nonmeteorological echoes, attenuation correction methods, the derivation of pseudo-constant-altitude plan position indicator (pseudo-CAPPI) images, the compositing of those images and the rainfall retrieval. Section 4 evaluates the performance of the attenuation correction algorithms, and section 5 highlights a number of discussion points. This paper ends with conclusions and some recommendations in section 6.

## 2. Data

### a. Radars

The Royal Netherlands Meteorological Institute (KNMI) operates two Gematronik METEOR 735CDP10 magnetron-based C-band dual-pol Doppler weather radars, located in the Netherlands, in Den Helder (52.953°N, 4.790°E, 51.0 m MSL, WMO code 6234) and Herwijnen (51.837°N, 5.138°E, 27.7 m MSL, WMO code 6356). They have an antenna diameter of 4.3 m, a wavelength of 5.326 cm (5.6 GHz), an antenna gain of 45 dB, a transmit peak power of 500 kW (250 kW per polarization), and a 3-dB beamwidth of 0.905°. Solar monitoring was employed to detect deviations in the pointings of the antennas as small as 0.05° (Beekhuis and Mathijssen 2018). Frequency-domain Doppler notch filtering with spectral reconstruction was applied to remove stationary echoes. A speckle filter was applied to remove isolated range bins with valid data surrounded by range bins with no data (Leijnse et al. 2016). Beekhuis and Mathijssen (2018) provide more information on these radars, such as the hardware calibration. The starting point for this study is the 16-bit volumetric data from both radars from the period 1430 UTC 3 August 2017–0800 UTC 31 July 2018, with a data availability of 98.8% and 99.1% for the radar in Den Helder and Herwijnen, respectively. Note that missing radar data were mainly caused by IT problems and planned maintenance, and rarely by malfunctioning radars. Every 5 min, the radars performed 16 azimuthal scans of 360°

around a vertical axis. Data from elevation scans 5 (2.0°), 6 (0.8°), and 7 (0.3°) were employed, since these are used for deriving operational radar precipitation products. Figure 1 displays the radar locations, as well as the volume coverage pattern for these elevation scans. Table 1 lists characteristics of the utilized elevation scans.

### b. Rain gauges

KNMI operates two rain gauge networks (Fig. 1). Hourly (each clock hour) rainfall depths were obtained from the automatic network of 32 gauges (density of ~1 gauge per 1000 km<sup>2</sup>). Daily (0800–0800 UTC) rainfall depths were obtained from the manual network of 322 gauges (density of ~1 gauge per 100 km<sup>2</sup>). These point (i.e., nongridded) data are employed for validation of hourly and daily rainfall depths from the corresponding radar pixel. In addition, daily in space interpolated rainfall depths from manual gauges were employed and accumulated to monthly and annual rainfall accumulations for the visual evaluation of radar rainfall maps. The automatic gauges are electronic ones that measure the precipitation depth using the displacement of a float placed in a reservoir, whereas the manual rain gauges are read by volunteers (KNMI 2000).

### c. Numerical weather prediction data

To allow for distinguishing between rain and other types of precipitation, the forecasted freezing-level height from the numerical weather prediction model HARMONIE-AROME (Bengtsson et al. 2017) cycle 38, as of 3 April 2018 cycle 40, was obtained. HARMONIE-AROME is a nonhydrostatic regional NWP model used operationally at KNMI and various other European weather centers. At KNMI, the HARMONIE-AROME model operates at 2.5 km × 2.5 km horizontal resolution and 65 vertical levels, and 48-h-long forecasts are initiated every three hours. For each cell and simulation output time-step, the first level for which the dry-bulb temperature reached at least 273.15 K was determined by scanning from the top of the atmosphere downward. In this study, the freezing-level height was computed by interpolation of the height of this level and the one above it, using their respective temperatures in the weighting. Because the freezing-level height will be employed to determine whether precipitation is liquid, in which case the air is (nearly) saturated, the dry-bulb temperature will be similar to the wet-bulb temperature. The subset covered the Netherlands and surroundings, coinciding with the radar coverage. The analysis was limited to data which would have been available in real time for coupling with real-time 5-min radar data, resulting in the use of the forecasts with +2-, +3-, +4-, or +5-h lead time, being available every 3 h. For instance, radar data with a time stamp of 0800–0825 UTC (representing the start time of the first elevation scan) were coupled with the 0600 UTC run with a +2-h lead time. Time stamps from 0830 to 0925 UTC were coupled with the +3-h lead time, from 0930 to 1025 UTC with the +4-h lead time, and from 1030 to 1055 UTC with the +5-h lead time.

### d. Disdrometers

An OTT Parsivel<sup>2</sup> disdrometer (e.g., Tokay et al. 2014) is installed at KNMI in De Bilt, as a replacement for the Parsivel

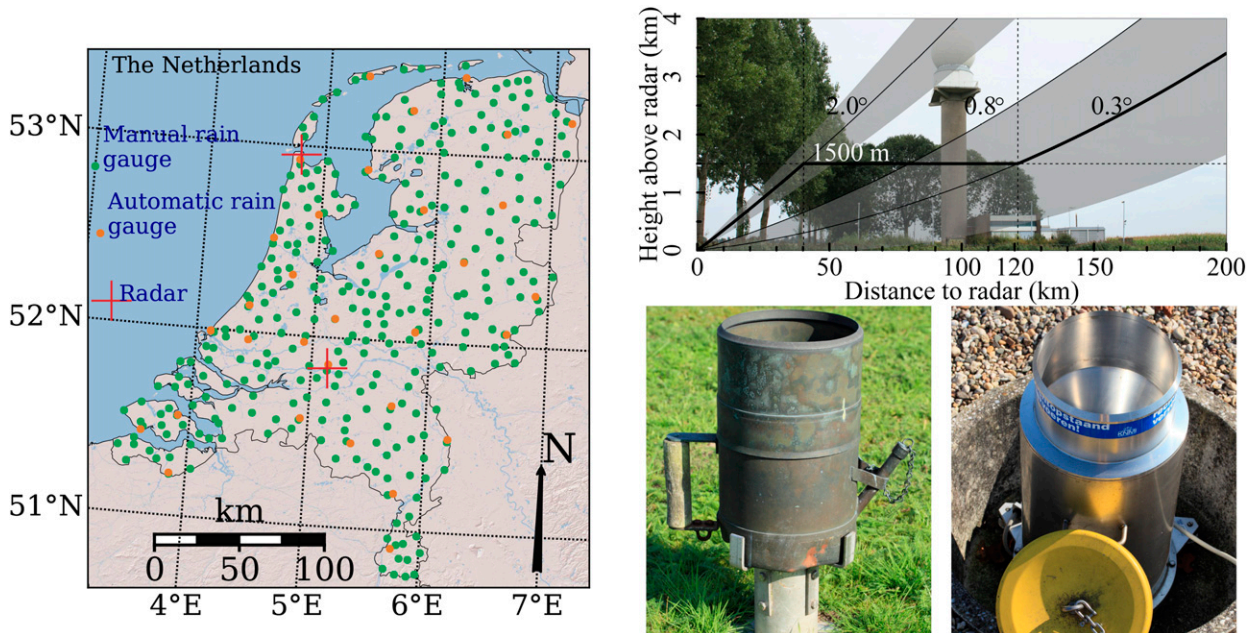


FIG. 1. (left) Map of the Netherlands with locations of KNMI's weather radars, and automatic and manual rain gauges. (top right) Volume coverage pattern showing the employed elevation scans and their height above the radar as a function of distance from the radar with the radar tower in Herwijnen in the background. The thick black line denotes the pseudo-CAPPI height, and the gray-shaded areas indicate the 1°-beam for the lowest and highest employed elevation scan. (bottom right) Photos of the manual and automatic rain gauge.

disdrometer used by [van de Beek et al. \(2016\)](#). Particle size distributions, rainfall intensity estimates, and precipitation type estimates from this instrument are available for the period between 8 January 2016 and 20 March 2020. All data were aggregated to a 1-min time scale, for which [Jaffrain and Berne \(2011\)](#) report a sampling uncertainty of 15% in terms of rainfall intensity. To only include rainfall in our analyses, and to minimize the effect of sampling, only data were used where the Parsivel indicates liquid precipitation, and where the maximum difference between rainfall intensities from the Parsivel and computed from the particle size distribution is 20%. This last step was taken to remove those 1-min samples for which the internal Parsivel algorithm has labeled a significant number of presumable raindrop detections as unreliable, thus increasing the quality of the dataset. Rainfall intensities  $R$  ( $\text{mm h}^{-1}$ ) were computed from the particle size distribution  $N(D)$  ( $\text{mm}^{-1} \text{m}^{-3}$ ) with the equation

$$R = 6 \times 10^{-4} \pi \int_0^{D_{\max}} v(D) D^3 N(D) dD, \quad (1)$$

where  $D$  (mm) is the raindrop diameter,  $v(D)$  ( $\text{m s}^{-1}$ ) is the terminal fall velocity of a raindrop from [Beard \(1976\)](#), and  $D_{\max}$  (mm) is the maximum raindrop diameter, which was set to 9 mm in this study.

### 3. Methods

The flowchart in [Fig. 2](#) provides an overview of the radar data processing chain. The starting point is the volumetric radar data from elevation scans 5, 6, and 7 (see [Table 1](#)) from the

two KNMI radars. First, the fuzzy logic echo classification and clutter identification based on polarimetric moments from the open-source Python library for weather radar data processing wradlib is applied ([Heistermann et al. 2013](#)). Subsequently, attenuation correction is employed either via the MK or via the Kdp method. [Figure 3](#) is used to illustrate the fuzzy logic and attenuation correction methods for one time interval with strong attenuation for the lowest elevation scan from the coastal radar in Den Helder. Next, 1500-m pseudo-CAPPI images of radar reflectivity factors are obtained for each radar, which are subsequently merged into one composite using range-weighted averaging (i.e., not  $\text{dBZ}_h$  values). Finally, 5-min rainfall intensities are retrieved from the horizontal reflectivity composites using the Marshall–Palmer  $Z_h$ – $R$  relation ( $Z_h = 200R^{1.6}$ ), which are accumulated to hourly, daily, monthly, and annual rainfall ([Wessels 1972](#); [Holleman 2006](#)).

TABLE 1. Technical characteristics of the employed radar elevation scans.

Characteristic	Scan 5	Scan 6	Scan 7
Elevation angle (°)	2.0	0.8	0.3
Pulse repetition frequency (Hz)	600 and 800	600 and 800	450
Pulse duration ( $\mu\text{s}$ )	1.49	1.49	2.66
Antenna rotation speed ( $^\circ \text{s}^{-1}$ )	24	24	12
No. of azimuths	360	360	360
No. of range bins	838	838	802
Range bin width (m)	223.5	223.5	399.0
No. of pulses per azimuth bin	~29	~29	~38

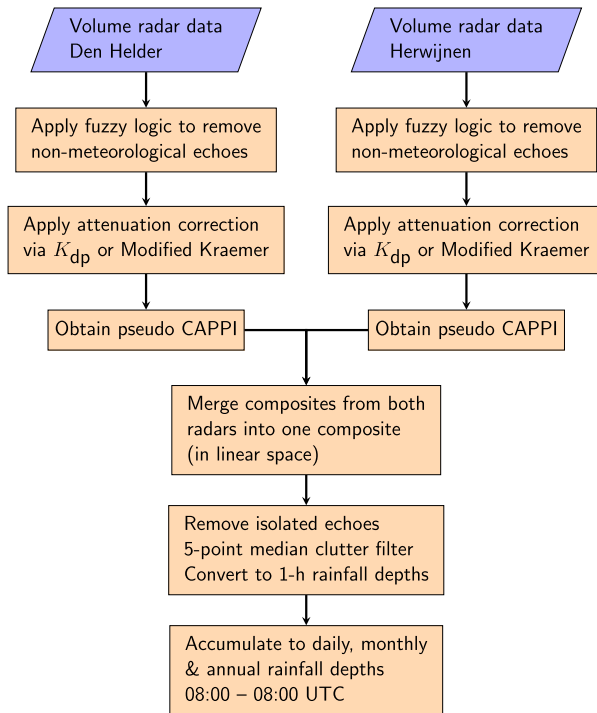


FIG. 2. Flowchart of radar data processing.

a. Nonmeteorological echo classification and removal

The function `clutter.classify_echo_fuzzy` from `wradlib` version 1.4.2 (Mühlbauer and Heistermann 2019) is employed to classify and remove nonmeteorological echoes from volumetric radar data. The fuzzy logic algorithm and settings from Overeem et al. (2020) are utilized, where the echo is assumed to be nonmeteorological in case the weighted average of the degree of membership to the meteorological target class is lower than a threshold value of 0.6. An illustration of the classification is provided in Fig. 3.

b. Classification of rain echoes with freezing-level height

The forecasted freezing-level height from the numerical weather prediction model HARMONIE-AROME, which would have been available in real time for the time stamp of the radar data, is employed to decide whether a  $Z_h$  value can be due to rain. The forecasts are used because of the latency due to the computation time of the model. For each radar voxel the height of the center of the radar beam is computed. If this height is below the freezing-level height, precipitation is assumed to be liquid. Due to storage issues of the HARMONIE data, these are not always available for coupling with radar data. In these cases, the volumetric radar data are not processed, resulting in a reduced availability of radar data, which becomes 92% over the entire period (318 days have data). Figure 3 shows for one time interval the freezing-level height and the radar beam height for the lowest elevation scan.

c. Attenuation correction via MK

PIA is only calculated with radar voxels below the forecasted freezing-level height. PIA is only added to  $Z_h$  for radar

voxels classified as meteorological. The MK method (Jacobi and Heistermann 2016) is a gate-by-gate attenuation correction based on the iterative approach of Hitschfeld and Bordan (1954) with two constraints: the maximum allowed  $Z_{h,cor}$  is 59 dBZ<sub>h</sub> and the maximum allowed PIA is 10 dB to avoid the risk of applying overly large corrections associated with numerical instabilities, which would result in a large overestimation of rainfall. Note that this is stricter than the value of 20 dB in Jacobi and Heistermann (2016), although a PIA of 10 dB is still large (a factor 10). MK outperforms other Hitschfeld–Bordan based attenuation correction algorithms for a 6-yr C-band weather radar dataset in southwest Germany (Jacobi and Heistermann 2016) and is implemented in the `wradlib` function `atten.correct_attenuation_constrained`, which is used in this study. The default value for `sector_thr` of 10 is employed, which is the number of adjacent beams for which the attenuation is recalculated in case the constraints are not met [see Jacobi and Heistermann (2016) for more details]. Figure 3 shows for one elevation scan and time interval that PIA only becomes 6 dB or larger, for certain azimuths experiencing moderate to heavy rain, which results in clearly higher values for  $Z_{h,cor}$ . The `wradlib` function `atten.correct_attenuation_constrained` requires an initial value for the linear coefficient  $\alpha$  of the  $k_h = \alpha Z_h^\beta$  relation (`a_max`) as well as a minimum allowed value in the downward iteration of  $\alpha$  if one of the constraints is not satisfied (`a_min`). It also requires an initial value for the exponent of the  $k_h = \alpha Z_h^\beta$  relation as well as a minimum allowed value in the downward iteration of  $\beta$  in case one of the two constraints is not met and  $\alpha$  has already reached its lower limit `a_min`. Values of  $\alpha$  and  $\beta$  are initially set to their maximum values, and are subsequently reduced until the conditions of  $Z_{h,cor} \leq 59$  dBZ and  $PIA \leq 10$  dB are met. The minimum number of iterations for  $\alpha$  (`n_a`) and  $\beta$  (`n_b`) is chosen as 100 and 6, respectively. More details are provided in `wradlib` (2020).

d. Attenuation correction via specific differential phase ( $K_{dp}$ )

The PIA is computed from the specific differential phase ( $K_{dp}$ ) employing the `wradlib` function `atten.pia_from_kdp` (Crisologo et al. 2014), and added to  $Z_h$ :

$$Z_{h,cor}(x) = Z_h(x) + 2\gamma \int_0^x K_{dp}(x) dx = Z_h(x) + PIA(x). \quad (2)$$

Note that the fuzzy logic algorithm is employed to set  $K_{dp}$  to 0 for nonmeteorological echoes, and that negative values of  $K_{dp}$  are also set to 0. In addition,  $K_{dp}$  is set to 0 if the radar voxel height is above the forecasted freezing-level height. This implies that in those cases involved radar voxel(s) do not contribute to the computation of PIA. Finally, the fuzzy logic algorithm is applied to remove nonmeteorological echoes from  $Z_{h,cor}$ , so PIA is only added to  $Z_h$  for radar voxels classified as meteorological. In this study,  $\gamma$  is assumed to be constant and no constraint on PIA is applied. Figure 3 shows for one elevation scan and time interval that PIA only becomes large for certain azimuths experiencing moderate to heavy rain, but generally much lower than for the MK attenuation correction method.  $K_{dp}$  has been derived from filtered differential

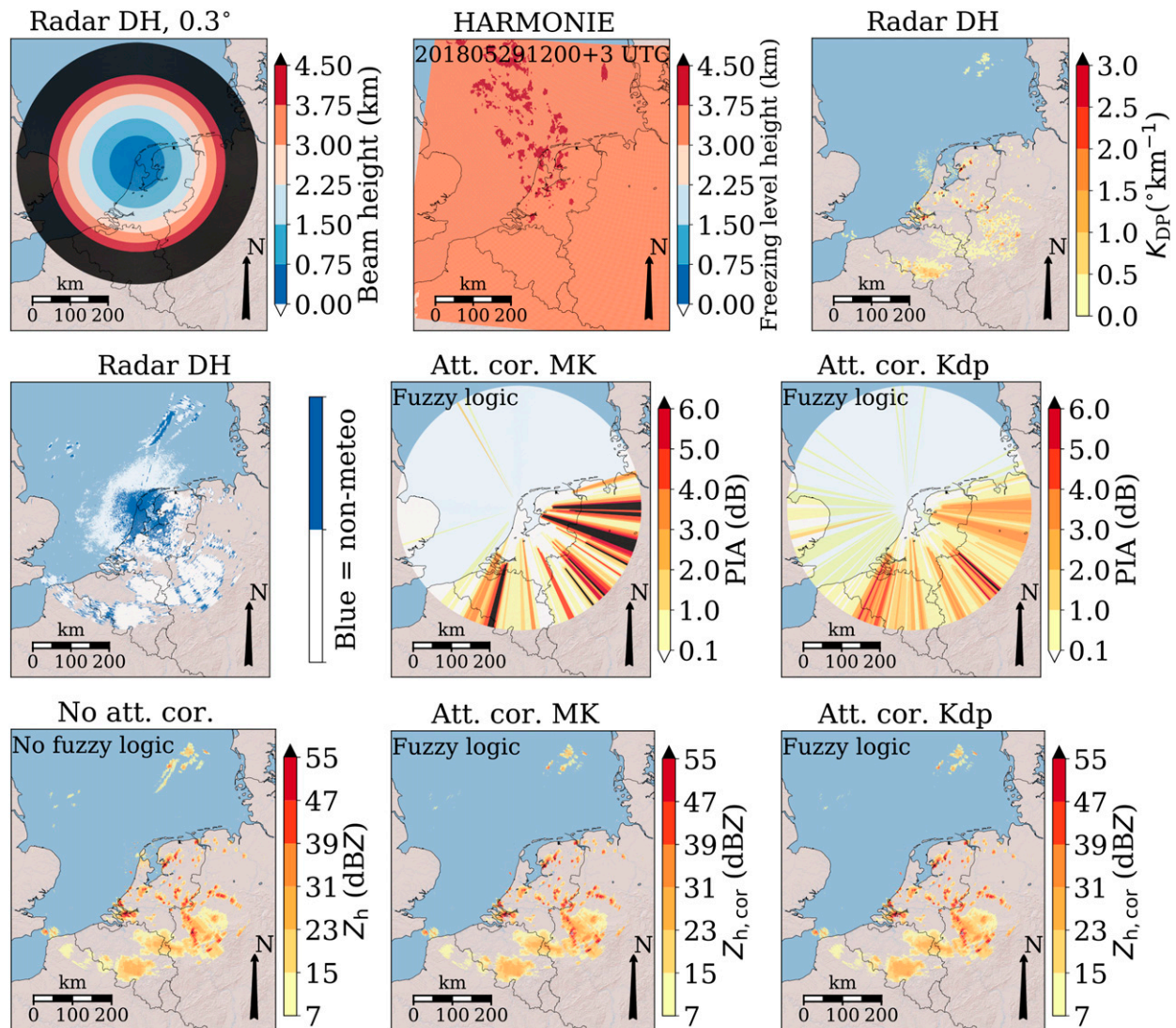


FIG. 3. Maps of the Netherlands and surroundings illustrating the attenuation correction procedures for 1500 UTC 29 May 2018 for data from the  $0.3^\circ$ -elevation scan from the coastal radar in Den Helder. (top left to top right) The height of the center of the radar beam, forecasted freezing-level height, and specific differential phase, respectively. (middle left to middle right) The classification result from the fuzzy logic algorithm and the computed PIA for the MK and the Kdp algorithms. (bottom) The radar reflectivity factors: (left)  $Z_h$ , for which no fuzzy logic and attenuation correction is applied; (center),(right) the computed PIA is added to this image to obtain  $Z_{h,cor}$ .

propagation phase ( $\Phi_{dp}$ ) data. The radar manufacturer's iterative finite impulse response (FIR) algorithm was applied, which removes rapid fluctuations (Hubbert and Brangi 1995). The  $\Phi_{dp}$  signal is low-pass filtered using a FIR filter with a 3-dB scale of 3 km (i.e., fluctuations in  $\Phi_{dp}$  on scales less than 3 km are effectively removed). When applying the FIR filter, a minimum signal-to-noise ratio of 3 dB, a minimum correlation coefficient of 0.8 and a maximum standard deviation of  $\Phi_{dp}$  of  $12^\circ$  is used. This filtered  $\Phi_{dp}$  is then used to compute  $K_{dp}$  values as range derivatives.

#### e. $k_h$ - $K_{dp}$ and $k_h$ - $Z_h$ relations

It is assumed here that the relations between horizontal specific attenuation  $k_h$  on the one hand and specific differential

phase  $K_{dp}$  and horizontal radar reflectivity factor  $Z_h$  on the other are power laws. Because the wradlib function `atten.pia_` from `kdp` only supports linear  $k_h$ - $K_{dp}$  relations, it is assumed that the exponent of this power law is equal to 1. The values of the coefficients and exponent of  $k_h = \gamma K_{dp}$  and  $k_h = \alpha Z_h^\beta$ , as well as their uncertainties, are estimated by employing values of  $k_h$ ,  $K_{dp}$ , and  $Z_h$  computed from disdrometer data (see section 2d).

Bulk radar variables are computed from 1-min drop size distributions (Brangi and Chandrasekar 2001) as in Leijnse et al. (2010), using T-matrix computations (Mishchenko 2000), with raindrop axis ratios from Andsager et al. (1999) and the complex refractive index of water from Liebe et al. (1991) at a temperature of  $15^\circ\text{C}$  (note that the effect of the temperature is

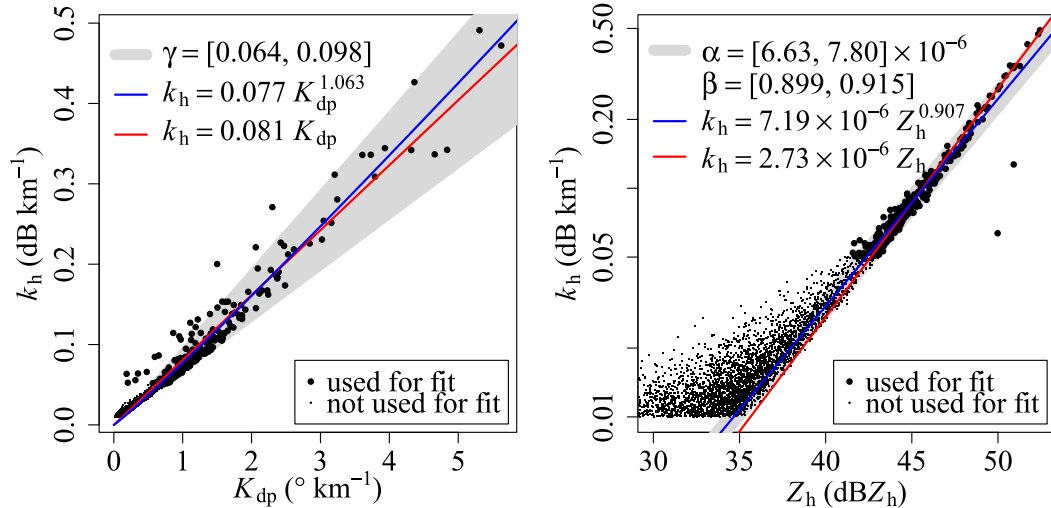


FIG. 4. Relations between (left)  $k_h$  and  $K_{dp}$ , and (right)  $k_h$  and  $Z_h$ . Power-law fits on these data are shown for the cases with (red) and without (blue) fixing the exponents at 1. Uncertainties about (left) the linear  $k_h$ - $K_{dp}$  relation and (right) the power-law  $k_h$ - $Z_h$  relation are shown in gray. Points not used for fitting these relations are shown as smaller dots.

small). Figure 4 shows how the specific horizontal attenuation  $k_h$  depends on  $K_{dp}$  and on  $Z_h$ . Power-law relations have been fitted on these data, with and without fixing the exponents to 1. All fits are limited to points with  $k_h \geq 0.05 \text{ dB km}^{-1}$  and  $Z_h \geq 30 \text{ dBZ}$  in order to derive relations valid for the most relevant range of values for this paper. The  $k_h$ - $Z_h$  relations are fitted based on logarithmic transforms of both  $k_h$  and  $Z_h$ . The resulting fits are also shown in Fig. 4. It is clear that the assumption of a linear  $k_h = \gamma K_{dp}$  relation holds. The resulting coefficient that is used in the remainder of this paper is  $\hat{\gamma} = 0.081 \text{ dB } (\text{°})^{-1}$  for the  $K_{dp}$  method.

The uncertainties in the relations that are used in this paper are estimated based on the errors that occur in the resulting estimates of  $k_h$ . For the linear  $k_h = \gamma K_{dp}$  relation, the errors in  $\gamma$  can be derived from  $k_h = (\hat{\gamma} + \varepsilon_\gamma)K_{dp}$ , so that

$$\varepsilon_\gamma = \frac{k_h}{K_{dp}} - \hat{\gamma}. \tag{3}$$

Equation (3) is evaluated for each data point so that the standard deviation of  $\varepsilon_\gamma$  can be estimated by taking the difference between the 0.16 and 0.84 quantiles of  $\varepsilon_\gamma$ , and dividing by 2. Note that for normally distributed variables this difference of quantiles is equal to the standard deviation. This method is used here because of its insensitivity to outliers. The value range, shown in Fig. 4, is  $\hat{\gamma} \pm 2\sigma_{\varepsilon_\gamma}$ . The same rationale is used for the uncertainties in the coefficient  $\alpha$  and exponent  $\beta$  of the  $k_h$ - $Z_h$  power law, where it is further assumed that the uncertainties in the  $\log(\alpha)$  and  $\beta$  are independent and contribute equally to the total uncertainty in  $\log(k_h)$ :

$$\varepsilon_{\log(\alpha)} = \frac{\log(k_h) - \log(\hat{\alpha}Z_h^\beta)}{2}, \tag{4}$$

$$\varepsilon_\beta = \frac{\log(k_h) - \log(\hat{\alpha}Z_h^\beta)}{2\log(Z_h)}. \tag{5}$$

The ranges of values of  $\alpha$  and  $\beta$  in Fig. 4 are  $\hat{\alpha} \exp[\pm 2\sigma_{\varepsilon_{\log(\alpha)}}]$  and  $\hat{\beta} \pm 2\sigma_{\varepsilon_\beta}$ . Hence, for the MK attenuation correction method the following values are used in the remainder of this study: a\_min:  $6.631 \times 10^{-6}$ ; a\_max:  $7.796 \times 10^{-6}$ ; b\_min: 0.899; b\_max: 0.915.

#### f. Pseudo-CAPPI per radar

For each radar horizontal cross sections of horizontally polarized radar reflectivity factors at constant altitude, called pseudo-CAPPIs, are constructed from the volumetric radar data. These pseudo-CAPPI images contain 8-bit reflectivity values, quantized in levels of  $0.5 \text{ dBZ}_h$ , at a 1-km spatial resolution. Figure 1 displays the volume coverage pattern, where the thick line denotes the pseudo-CAPPI at 1500 m. For the first 40 km from the radar only data from the  $2.0^\circ$  elevation are used. For the domain from 40 to 121 km from the radar, the pseudo-CAPPI is constructed by linear interpolation of the reflectivity values ( $\text{dBZ}_h$ ) of the nearest elevation below and above the 1500-m height. This interpolation is done in logarithmic space, which is the default method in operational radar processing software, to further reduce the influence of non-meteorological echoes. Only the reflectivity values of the lowest elevation are used for areas beyond 121 km from the radar, where it crosses the height of 1500 m.

#### g. Compositing pseudo-CAPPI images

The pseudo-CAPPI images from the individual radars are combined into one composite using range-weighted compositing, where reflectivities close to the radar are assigned lower weights to limit the impact of bright bands and spurious echoes, i.e., the other radar is assigned higher weights. This compositing



method prevents the occurrence of discontinuities in the radar-derived rainfall images in the vicinity of the radar and at the edge of the coverage of a radar (Overeem et al. 2009). Composites are only obtained if the pseudo-CAPPIs from both radars contain data, in which case the reflectivity values are linearly averaged, i.e., the arithmetic mean is computed.

#### h. Rainfall retrieval

Reflectivities below  $7 \text{ dBZ}_h$  ( $\sim 0.1 \text{ mm h}^{-1}$ ) are not converted to rainfall intensities to avoid the accumulation of noise. Reflectivities above  $55 \text{ dBZ}_h$  ( $\sim 100 \text{ mm h}^{-1}$ ) are set to  $55 \text{ dBZ}_h$  to reduce the influence of echoes induced by hail or strong residual clutter. Isolated pixels are those for which none of the eight neighboring pixels have values  $\geq 7 \text{ dBZ}_h$ . They are not used in the conversion to rainfall intensity, but are set to  $0 \text{ mm h}^{-1}$ . Next, the reflectivities  $Z_h$  ( $\text{mm}^6 \text{ m}^{-3}$ ) of the pseudo-CAPPI images are converted to rainfall intensities  $R$  ( $\text{mm h}^{-1}$ ) with the fixed  $Z_h$ - $R$  relationship (Marshall et al. 1955), independent of season or type of rain,

$$Z_h = 200R^{1.6}, \quad (6)$$

implicitly assuming an exponential drop size distribution, Rayleigh scattering and a power law for the terminal fall speed of drops as a function of diameter. With  $0.5 \text{ dBZ}_h$  classes this results in 97 possible levels of rainfall intensities ranging from  $0.1$  to  $100 \text{ mm h}^{-1}$ . One-hour rainfall accumulations are constructed from the 5-min rainfall intensities if at least 10 images (minimum availability of 83.3%) are available. Local outliers caused by accumulated residual clutter are removed from the hourly accumulations using a 5-pixel median filter on nearest-neighbor pixels. If one or two images are missing, the 1-h accumulated rainfall is scaled by the fraction of available images. Next, only data from days are used for which the data availability of the corresponding 24-h (0800–0800 UTC) period is at least 83.3%. In case of a lower availability, the hourly or daily radar data as well as the corresponding gauge data are not considered in the comparisons presented here. These minimum availabilities are demanded to allow a fair comparison with rain gauge accumulations. Note that data availability is only affected by the existence of entire composites and is not computed per pixel. Echoes that have been removed are effectively set to  $0 \text{ mm h}^{-1}$  and do not affect the reported data availability. The resulting data availability of the images containing hourly and daily rainfall depths are 87.4% and 87.8%, respectively (0800 UTC 3 August 2017–0800 UTC 31 July 2018). Also a dataset without an attenuation correction is evaluated. To base this dataset on the same period as the corrected ones, only composited pseudo-CAPPI images are employed for which the corresponding one from the Kdp method has data.

## 4. Results

Evaluations against rain gauge data are presented for three radar rainfall datasets: 1) no attenuation correction, 2) attenuation correction with MK method, and 3) attenuation correction with Kdp method. Note that it is not the aim of this study to unravel all specific sources of error causing differences

between gauge and radar data (Hazenberg et al. 2011, 2013; van de Beek et al. 2016).

#### a. Annual and monthly rainfall accumulations

First, a general impression of the improvement in QPE for the MK and Kdp methods is given. Annual and selected monthly rainfall maps are presented in Fig. 5. The first column shows the maps based on interpolated manual rain gauge data. The second column reveals a severe underestimation in the radar rainfall maps which have not undergone attenuation correction. In general, radar rainfall maps are in better agreement with the gauge-based ones if the MK method (third column) is applied. QPE shows an even larger improvement when the Kdp method (fourth column) is utilized. Though improvements in the annual rainfall maps are relatively modest (first row), larger improvements are found for monthly rainfall maps (second, third, and fourth row), where the Kdp attenuation correction method performs better than the MK attenuation correction method. July 2018 shows small rainfall depths, but persistent nonmeteorological echoes above sea, mainly related to shipping to the ports of Rotterdam (the Netherlands) and Antwerp (Belgium). From August 2017 and April 2018 one could conclude that echoes due to maritime transport are amplified by the attenuation correction methods, but July 2018 shows that nonmeteorological echoes are not clearly amplified.

#### b. Verification of hourly and daily rainfall depths

An independent verification of daily (0800–0800 UTC) and hourly radar rainfall depths against rain gauges is performed to quantify the influence of the attenuation correction algorithms on QPE. Table 2 shows metrics for the relative bias of radar rainfall depths compared to the corresponding gauge rainfall depths, the residual standard deviation, the Pearson correlation coefficient ( $\rho$ ) and the mean absolute error for daily rainfall. Here, a residual is defined as the radar rainfall depth minus the gauge rainfall depth. Results are presented for all values and for those where radar and/or gauge exceed specific thresholds. Note that all selected values are used to compute the metrics. A number of conclusions can be drawn from Table 2: 1) severe underestimation of rainfall by 47.6%–51.1% without attenuation correction; 2) the average underestimation is  $\sim 3$ –9 and  $\sim 7$ –14 percentage points lower for the MK and the Kdp method, respectively, compared to a reference without attenuation correction. Underestimation decreases for increasing rainfall depths for both methods; 3) the residual standard deviation slightly decreases without threshold and for the 0.1-mm threshold, it slightly increases for the 10.0-mm threshold, but it strongly increases for the 20.0-mm threshold (likely related to the much higher variability for larger rainfall depths); 4) generally a slight decrease in  $\rho$  is found compared to the case without attenuation correction (likely related to decreasing range of rainfall values); 5) MAE decreases slightly without threshold and for the 0.1-mm threshold, but it shows a strong reduction for the larger rainfall depths, especially for the Kdp method.

Figure 6 shows scatter density plots where only radar–gauge pairs are used for which the gauge rainfall depths are above

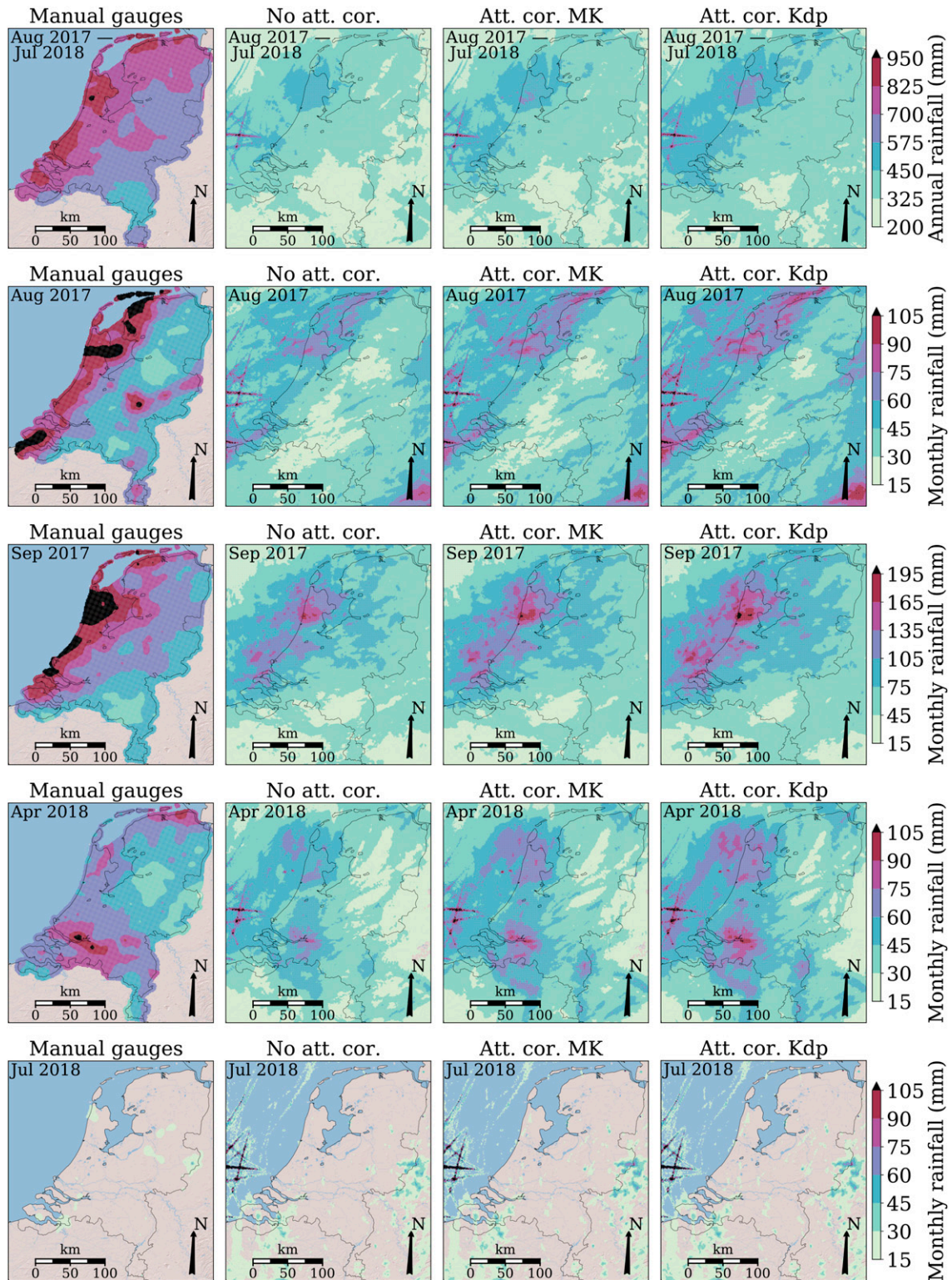


FIG. 5. Maps of (first row) annual (0800 UTC 4 Aug 2017–0800 UTC 31 Jul 2018) and (remaining rows) monthly rainfall accumulations for the Netherlands and surroundings based on interpolated data from (first column) ~322 manual rain gauges and radar rainfall composites: (second column) no attenuation correction, (third column) MK attenuation correction, and (fourth column) Kdp attenuation correction. A month runs from 0800 UTC on the last day of the previous month up to 0800 UTC on the last day of the present month.

TABLE 2. Validation of 24-h 0800 UTC rainfall accumulations of radar composites. Mean daily rainfall depth of the manual rain gauges, bias, residual standard deviation (std dev), Pearson correlation coefficient, and mean absolute error (MAE) are given for the validation with the manual rain gauge network over the period 3 Aug 2017–31 Jul 2018. Threshold means that radar and/or gauge are above the threshold value. Results are shown without attenuation correction and with MK and Kdp attenuation correction.

Threshold (mm)	Mean (mm)	Relative bias (%)	Std dev (mm)	Correlation	MAE (mm)
No attenuation correction					
	2.29	−48.8	2.75	0.88	1.29
0.1	4.18	−48.9	3.46	0.85	2.35
10.0	16.96	−51.1	5.49	0.71	9.01
20.0	28.33	−47.6	7.40	0.58	13.98
Attenuation correction: MK					
	2.29	−45.7	2.65	0.86	1.25
0.1	4.18	−45.7	3.35	0.84	2.28
10.0	16.84	−45.5	5.90	0.69	8.43
20.0	28.00	−38.8	8.79	0.52	12.39
Attenuation correction: Kdp					
	2.29	−42.2	2.53	0.87	1.20
0.1	4.17	−42.2	3.21	0.85	2.18
10.0	16.78	−41.3	5.86	0.70	7.84
20.0	27.88	−33.9	8.74	0.54	11.18

1 mm. The first row shows the results for daily rainfall over the entire period. Differences in the values for the coefficient of variation (CV) and  $\rho^2$  are small, but the underestimation decreases from 50.8% to 47.6% (MK) or 44.1% (Kdp), and values are much closer to the 1:1 line after attenuation correction. To study seasonal differences in performance, scatter density plots are also provided for the winter months (row 2) and the summer months (row 3). In the winter months only a reduction of a few percentage points in the underestimation is found for the Kdp method. In many cases the radar beam will be above the forecasted freezing-level height, where precipitation is usually not liquid. Hence, the attenuation correction is not applied in these cases. For the MK method the improvement is even negligible, which was also found by Hazenberg et al. (2011) for a region in Belgium. The highest rainfall intensities generally occur in the summer months, where attenuation is expected to play a larger role. The underestimation decreases from 36.6% to 30.8% (MK) or 26.5% (Kdp), where the other metrics only show slight differences for the MK method and small improvements for the Kdp method. Moreover, the values are much closer to the 1:1 line.

Table 3 has the same layout as Table 2, but shows the validation of hourly rainfall accumulations. The following conclusions can be drawn: 1) severe underestimation of rainfall by 43.9%–54.7% without attenuation correction; 2) the average underestimation is ~3–15 and ~7–18 percentage points lower for the MK and the Kdp method, respectively, where underestimation is lowest for the two highest thresholds; 3) the residual standard deviation slightly decreases without threshold and for the 0.1-mm threshold, but generally increase more strongly for the larger rainfall depths; 4) For the MK method  $\rho$  stays constant or slightly decreases, whereas for the Kdp method always a small increase is found; 5) MAE stays equal or decreases slightly without threshold and for the 0.1-mm threshold, but displays a stronger reduction for the larger rainfall depths, especially for the Kdp method.

The fourth row in Fig. 6 shows scatter density plots for hourly rainfall over the entire period. The underestimation decreases from 52.2% to 47.4% (MK) or 43.7% (Kdp), and values are much closer to the 1:1 line. Improvements in the values for CV and  $\rho^2$  are found when applying the Kdp method, whereas values for the MK method only improve marginally.

Generally, both attenuation correction algorithms clearly improve QPE, especially in terms of bias. Notably better results are obtained for the Kdp method compared to the MK method.

### c. Case studies

Case studies of daily and hourly rainfall depths are presented to exemplify the performance of the attenuation correction methods. Figure 7 presents daily rainfall maps based on interpolated rain gauge data and based on radar data excluding and including attenuation correction. Row 1 shows a day (0800 UTC 8 September–0800 UTC 9 September 2017) with a mixture of convective and stratiform rainfall, where the attenuation correction algorithms improve QPE, especially for the Kdp method. Still, there are large underestimations with respect to the gauge-based map, which may be due to a variety of sources of error, such as vertical profile of reflectivity, sub-optimal values of the coefficients in the  $Z_h$ – $R$  relationship, and radome attenuation (Hazenberg et al. 2011). Row 2 presents a severe convective case (0800 UTC 29 May–0800 UTC 30 May 2018), where the underestimations without attenuation correction transform to overestimations in the northern part of the country, especially for the Kdp method. This is investigated in more detail with the scatter density plots in Fig. 8, evaluating the daily and hourly radar rainfall depths against the gauge-based ones. All radar–gauge pairs from this day are compared at the rain gauge locations, taking into account only those pairs where the gauge measures more than 1 mm. First, daily rainfall is evaluated (first row). A strong underestimation of 21.2% is found without attenuation correction. Application of the

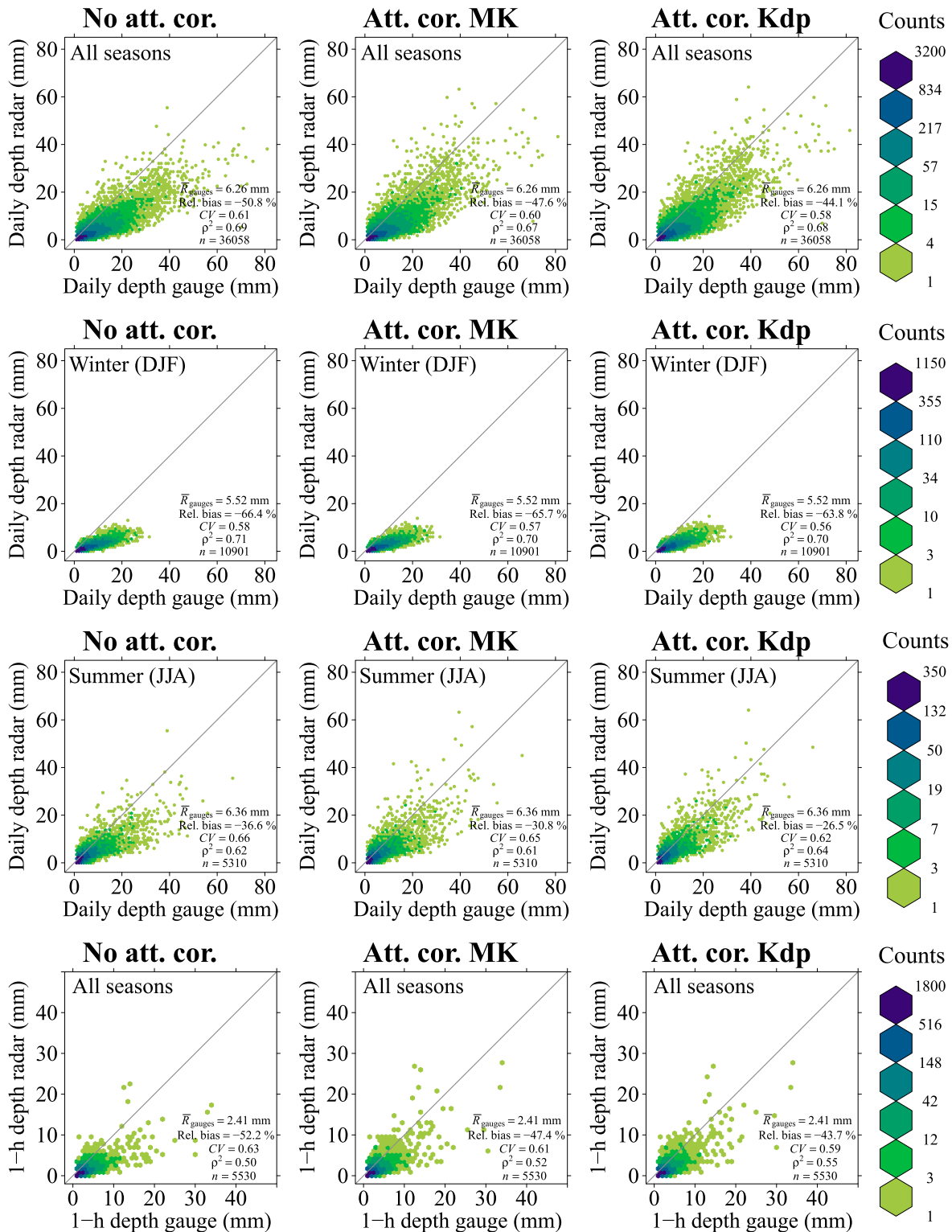


FIG. 6. Scatter density plots of daily (0800–0800 UTC) and hourly (clock hour) composited radar rainfall accumulations against the manual and automatic gauge accumulations, respectively, for 0800 UTC 4 Aug 2017–0800 UTC 31 Jul 2018. Binned in 1-mm intervals. For radar–gauge pairs where gauge rainfall > 1 mm. Verification for daily rainfall over the entire period, (second row) the winter months, and (third row) the summer months. (fourth row) Verification for hourly rainfall over the entire period. The number of pairs is represented by  $n$ .  $\bar{R}_{\text{gauges}}$  is the average daily or 1-h gauge rainfall depth.

TABLE 3. Validation of 1-h (clock hour) rainfall accumulations of radar composites. Mean hourly rainfall depth of the automatic rain gauges, bias, residual standard deviation, Pearson correlation coefficient, and mean absolute error are given for the validation with the automatic rain gauge network over the period 3 Aug 2017–31 Jul 2018. Threshold means that radar and/or gauge are above the threshold value. Results are shown without attenuation correction and with MK and Kdp attenuation correction.

Threshold (mm)	Mean (mm)	Relative bias (%)	Std dev (mm)	Correlation	MAE (mm)
No attenuation correction					
	0.09	-43.9	0.31	0.82	0.06
0.1	0.82	-45.1	0.90	0.76	0.51
5.0	8.22	-51.5	3.77	0.50	4.71
10.0	14.67	-54.7	5.28	0.38	8.57
Attenuation correction: MK					
	0.09	-40.5	0.30	0.81	0.06
0.1	0.82	-41.6	0.87	0.76	0.50
5.0	7.98	-38.6	4.07	0.50	4.20
10.0	14.37	-39.5	6.19	0.36	7.15
Attenuation correction: Kdp					
	0.09	-36.6	0.29	0.83	0.05
0.1	0.81	-37.7	0.83	0.78	0.49
5.0	7.90	-34.2	3.88	0.53	3.83
10.0	14.26	-36.5	5.71	0.42	6.51

attenuation correction algorithms leads to an overestimation of 3.1% (MK) or 7.5% (Kdp), and the value for CV slightly decreases. The value for  $\rho^2$  increases from 0.53 to 0.58 (MK) or 0.61 (Kdp). Next, hourly rainfall is evaluated (second row). A strong underestimation of 32.9% is found without attenuation correction. Application of the attenuation correction algorithms leads to an underestimation of 12.1% (MK) or 3.8%

(Kdp), and the value for CV strongly decreases from 0.75 to 0.63 (MK) or 0.54 (Kdp). The value for  $\rho^2$  remains almost the same for MK (0.70), but increases for Kdp (0.78). The attenuation correction methods are effective in improving hourly and daily QPE, where the Kdp method performs best, except for the larger overestimation for daily rainfall. Note that part of the differences between radars and gauges will be related to

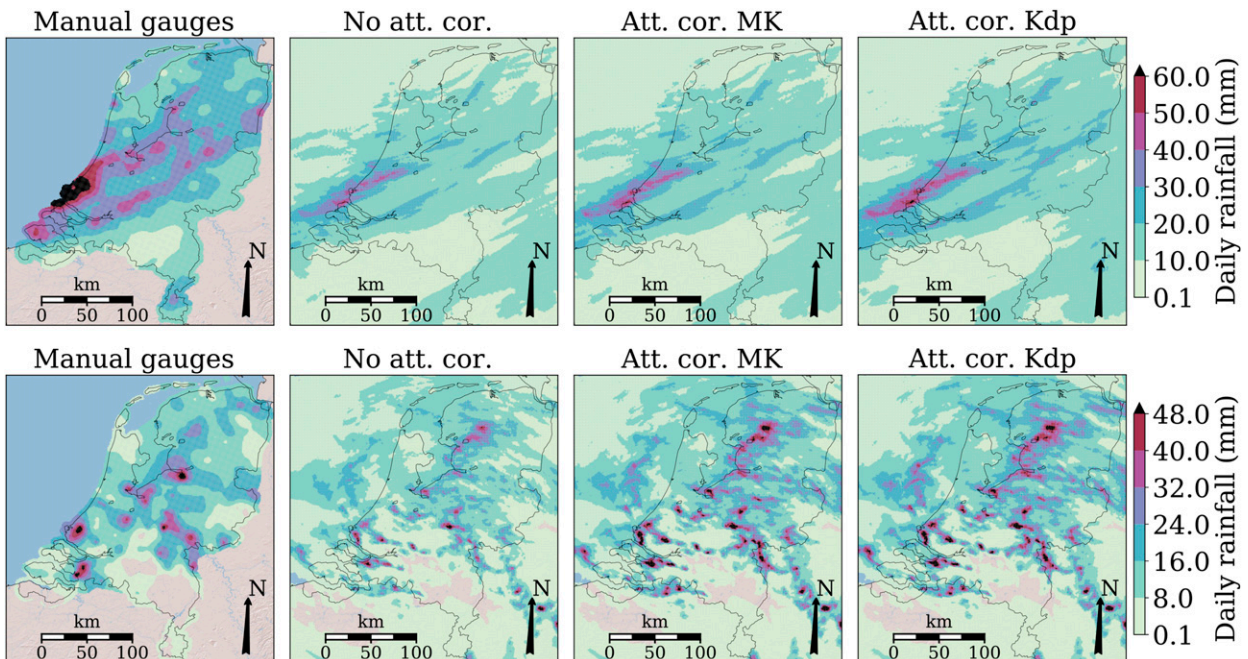


FIG. 7. Maps of daily rainfall accumulations for the Netherlands and surroundings for (top) 0800 UTC 8 Sep–0800 UTC 9 Sep 2017 and (bottom) 0800 UTC 29 May–0800 UTC 30 May 2018. Based on interpolated data from (first column) ~322 manual rain gauges, and radar rainfall composites: (second column) no attenuation correction, (third column) MK attenuation correction, and (fourth column) Kdp attenuation correction.

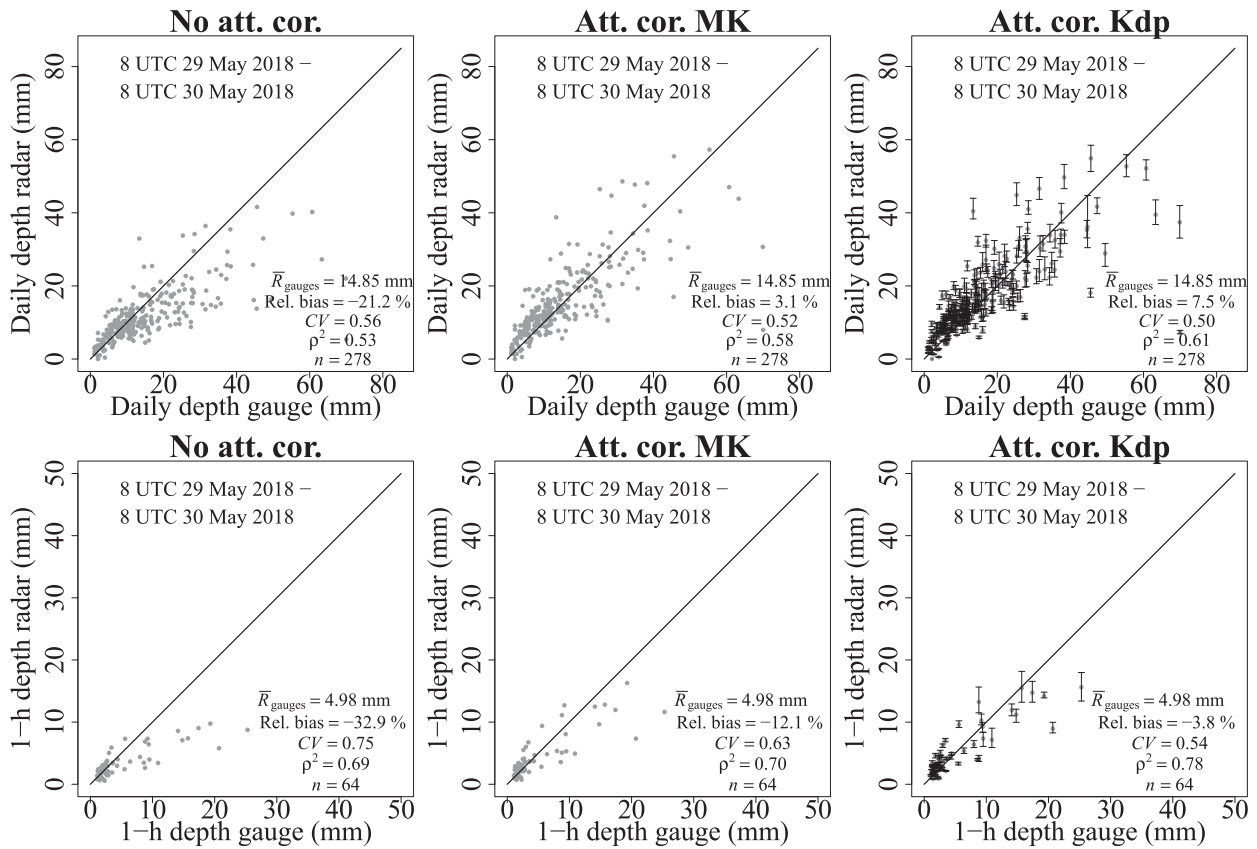


FIG. 8. Scatterplots of (top) daily (0800–0800 UTC) and (bottom) hourly (clock hour) composited radar rainfall accumulations against the manual and automatic gauge accumulations, respectively, for 0800 UTC 29 May–0800 UTC 30 May 2018. Binned in 1-mm intervals. For radar–gauge pairs where gauge rainfall > 1 mm. Verification without (left) attenuation correction, (center) MK attenuation correction, and (right) Kdp attenuation correction, for which also uncertainty due to applying a minimum and maximum value for  $\gamma$  is presented by the vertical lines. The number of pairs is represented by  $n$ .  $\bar{R}_{\text{gauges}}$  is the average daily or 1-h gauge rainfall depth.

representativeness errors. This day displays large spatial rainfall variability. The localized showers can easily be missed by a rain gauge, where the radar still captures the event due to its much larger measurement volume. On the other hand, a gauge may also record a higher local rainfall depth than the radar volume. Finally, also precipitation advection and the application of a five-point median clutter filter may play a role here.

d. Comparison between radars

Polar data from the three elevation scans (Table 1) are employed to compare  $Z_h$  from the radar in Herwijnen with the one in Den Helder. The aim is to assess the ability of the Kdp method to decrease differences in  $Z_h$  between both radars. Though none of the radars can be assumed to be the truth, attenuation will likely lead to larger differences between the two as the path through which the signals propagate, and hence the attenuation, is different for both radars. Hence, it also provides an estimate of the extent to which differences can be attributed to rain-induced attenuation. As an aside, such an assessment would also reveal systematic differences which may be due to hardware calibration errors.

Polar data from both radars are collocated by employing the Intercomparison function from the Rain Scientific Data

Analysis and Display (RainSNIP; version 3.2.1) tool from Leonardo Germany GmbH. Only elevation scan data within 4 min (“trust time interval”), within a 200-m altitude difference of the center of the beams (“trust height interval”), and a ratio between the volumes of the two voxels from the radars of up to 1.3 (“trust volume ratio”) are considered. In addition, only pairs are selected where both  $Z_h$  values are in the range 0–95.5 dBZ<sub>h</sub>.

The output files of RainSNIP are used to make scatter density plots of  $Z_h$ , comparing the radar in Herwijnen with that in Den Helder, where only pairs are considered having at least one  $Z_h$  value of 7 dBZ<sub>h</sub> or higher. Only those cases are selected where at least one of the radars experiences substantial attenuation ( $\geq 3$  dB). This is determined by computing the difference between attenuation-corrected and uncorrected  $Z_h$  for each radar and voxel separately.

Each column in Fig. 9 represents results from one season. The first row shows results without attenuation correction, whereas the second row shows results for the Kdp method. In general, differences between both radars are quite large, revealing appreciable scatter and biases ranging from 1.1 dB (winter) to 2.0 dB (autumn). Application of the Kdp attenuation correction slightly increases the bias from 1.2 to 1.4 dB

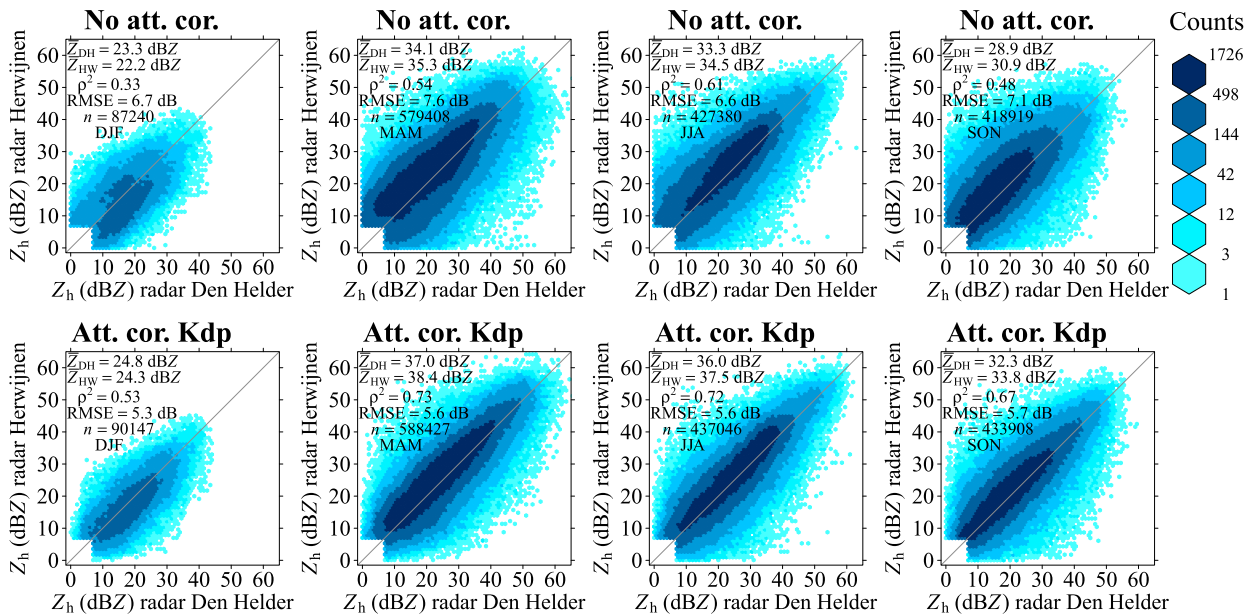


FIG. 9. Scatter density plots of  $Z_h$  comparing the radar in Herwijnen with the one in Den Helder. Each column represents one season. (top) Without attenuation correction and (bottom) with Kdp attenuation correction. (left to right) Columns show the seasons: winter (December–February), spring (March–May), summer (June–August), and autumn (September–November), respectively. Only those cases where at least one of the radars experienced substantial attenuation ( $\geq 3$  dB) were selected.

(spring), and from 1.2 to 1.5 dB (summer), whereas it is reduced from 1.1 to 0.5 dB (winter) and from 2.0 to 1.5 dB (autumn). Remaining biases after attenuation correction point to other sources of error. Remaining hardware calibration errors and wet radome attenuation could play a role here. Since the criteria to match polar data from both radars are rather strict in order to assure a fair comparison in time and space, representativeness errors are expected to play a limited role. Since the radars are virtually sampling the same volume at similar range, other sources of error are expected to influence the data from both radars in a similar way, hence not leading to differences. Apart from the biases, attenuation correction clearly improves the correspondence in  $Z_h$  between both radars: the value for  $\rho^2$  increases strongly and the value for RMSE reduces by 1.0–2.0 dB.

## 5. Discussion

### a. Coefficients $k_h$ – $K_{dp}$ and $k_h$ – $Z_h$

The coefficients of the  $k_h$ – $K_{dp}$  and  $k_h$ – $Z_h$  relationships are based on a large disdrometer dataset. Since raindrop size distribution and raindrop temperature can vary considerably in space and time (see Fig. 4), the employed coefficients will not be optimal for every event or even ray or time interval. This is expected to be less important for  $k_h$ – $K_{dp}$  given the near-linearity of this relationship, thus being less sensitive to variability in the drop size distribution. Uncertainties in the MK attenuation correction may be larger due to the nonlinearity. Figure 8 presents the range of rainfall estimates due to uncertainty in the value of  $\gamma$  (third column), where a minimum [0.064 dB ( $^\circ$ ) $^{-1}$ ] and a maximum [0.098 dB ( $^\circ$ ) $^{-1}$ ] value was

obtained from section 3e. Differences can become relatively large for the larger hourly or daily rainfall depths from this day. Note that the disdrometer data were not employed to estimate the coefficients of the  $Z_h$ – $R$  relationship and their uncertainties. However, the employed coefficients provide a good fit to bulk variables as computed from observed drop size distributions from the Netherlands (Wessels 1972; Holleman 2006), and are used in KNMI’s operational radar precipitation products (Holleman 2007; Overeem et al. 2009). Moreover, these coefficients are commonly applied for radars in temperate climates.

The typical range of  $\gamma$  for C-band radars is 0.05–0.18 dB ( $^\circ$ ) $^{-1}$  (Trömel et al. 2014; Ryzhkov et al. 2014). The average climatological value of 0.081 dB ( $^\circ$ ) $^{-1}$ , found in this study, and based on a 4-yr disdrometer dataset, is consistent with Carey et al. (2000) for a tropical climate, which was applied by Crisologo et al. (2014) to C-band radar data from a tropical climate. Vulpiani et al. (2012) apply this same value to data from two C-band radars from mountainous areas in Italy for a preliminary attenuation correction, where the temperature profile from the nearest radio sounding is used to roughly identify rain. Next, they perform a hydrometeor classification. Subsequently, the  $Z_h$  values are corrected for attenuation by utilizing different values of  $\gamma$  for light, moderate, heavy, or large drops from which an optimal value for  $\gamma$  is computed at each range distance. This approach is similar to the one employed by Vulpiani et al. (2008), although they employ a Bayesian approach for hydrometeor classification which does not use temperature data. Such a method, where the hydrometeor classification precedes the attenuation correction, may help to select a more appropriate value of  $\gamma$ . By employing

the air temperature from a numerical weather prediction model, the values for  $\gamma$  could even be chosen as a function of temperature.

### b. Freezing-level height and rainfall detection

Since the attenuation correction methods are meant to correct for rain-induced attenuation, they should only be applied to radar voxels with precipitation in the form of rain. Volumetric radar data could reveal the height of the melting layer, where all precipitation below it can be assumed to be rain. However, such a melting layer can only be detected in case it occurs closer to the radar, because the radar beam height increases as a function of range from the radar.

Alternatively, air temperature observations could be employed, but radiosonde soundings are sparse in time and space. In addition, the more abundant surface temperature observations could be combined with an assumed lapse rate to estimate air temperatures aloft, but this also comes with uncertainties. Mode-S observations from tracking and ranging air traffic control radars also contain information on temperature (de Haan and Stoffelen 2012) and could possibly be useful for this purpose, but profiles are mostly available near airports and much reduced during the night. The forecasted freezing-level height from HARMONIE-AROME has been used because it always provides an estimate for the entire radar domain, with a reasonable temporal resolution of 1 h and with a high spatial resolution of 2.5 km. Uncertainties in this approach are 1) the forecasted freezing-level height may not be representative of the true freezing-level height; 2) it is assumed that echoes below the freezing-level height are rain, whereas still solid or melting precipitation or a mixture of precipitation types may exist below the freezing-level height; 3) the center of the radar beam is used to compare with the freezing-level height, whereas part of the beam may be above and below the freezing-level height. Hence, echoes may stem from different precipitation types. Given points 2) and 3) it might be better to use the height of the lower half-power point of the beam pattern; 4) the forecasted freezing-level height is available every hour and the closest forecast is collocated with the 5-min polar radar data. This implies that in case of strong temporal variability of the freezing-level height errors will occur. To improve the classification of rain, a hydrometeor classification could be preceded or succeeded by a classification based on the HARMONIE-AROME freezing-level height. Alternatively, the hydrometeor classification could be fed with air temperature data from a numerical weather prediction model.

The freezing-level height based on dry-bulb temperature is used, which is expected to be quite close to the freezing-level height based on wet-bulb temperature in case of precipitation (i.e., a saturated atmosphere). A case study based on HARMONIE model data (not shown) reveals that freezing-level height based on dry-bulb temperature displays much smaller spatial variability. Since it is difficult to capture the exact location of precipitation in numerical weather models, we expect that the lower spatial variability in the dry-bulb freezing-level height makes our analyses less vulnerable to inaccuracies in the location and timing of precipitation by HARMONIE compared to using a wet-bulb temperature.

Hence, the dry-bulb freezing-level height from NWP will be more representative of the actual wet-bulb temperature in precipitation, especially in case of a spatial mismatch between model and actual precipitation.

### c. Comparison with other studies

Relatively few studies evaluate attenuation correction algorithms on large datasets, and none of them compare single- and dual-pol based attenuation correction methods. Moreover, different radar bands (C, S, or X), climates, employed metrics and thresholds hinder an exact comparison. For instance, attenuation will be much more pronounced at lower latitudes, allowing for larger relative improvements in QPE due to attenuation correction. In addition, relative improvements with respect to QPE without attenuation correction also depend on the initial quality of the radar products. This can be different due to differences among radars and processing algorithms.

Crisologo et al. (2014) provide an evaluation of the Kdp-based wradlib algorithm against accumulations from 16 rain gauges over a 5-month period employing almost the same value for  $\gamma$ ,  $0.08 \text{ dB } (^{\circ})^{-1}$  for a C-band radar in a tropical climate (the Philippines). Most apparent is the decrease in the underestimation from 43.4% to 13.7% for daily and from 45.7% to 15.8% for hourly rainfall, as well as the decrease in the residual standard deviation from 25.4 to 17.8 mm and the increase in the Nash–Sutcliffe efficiency from 0.54 to 0.8, both for daily rainfall. This much stronger improvement compared to this study has to be caused by attenuation being more dominant as a source of error in tropical climates. This is even true when compared to the results for the summer months in the Netherlands, which often experience convective rainfall.

Figueras i Ventura et al. (2012) evaluate a Kdp-based attenuation correction employing a linear relation between differential phase and  $k_h$  for five radars in France within a 60-km range from the radars comparing with typically between 30 and 50 rain gauges per radar. The C-band radar in Avesnes in northern France is expected to have a similar climate as the Netherlands. They employ almost the same value for  $\gamma$ ,  $0.08 \text{ dB } (^{\circ})^{-1}$ . Based on five rainfall events from the Avesnes radar (844 pairs) from July and August 2010, they find that the relative bias improves from  $-53\%$  to  $-43\%$  when applying the Kdp-based attenuation correction in combination with the same  $Z_h$ – $R$  relationship as used in this study, for hourly rain gauge depths larger than 1 mm. In addition, the correlation coefficient improves from 0.71 to 0.84. Based on four rainfall events from the Trappes radar (729 pairs) from July and August 2010, they find that the relative bias improves from  $-25\%$  to  $-10\%$  when applying the Kdp-based attenuation correction, again using the same  $Z_h$ – $R$  relationship for hourly rain gauge depths larger than 1 mm. In addition, the correlation coefficient improves from 0.80 to 0.86. A fair comparison with these metrics is provided by discussing the results for the scatter density plots for hourly rainfall in the summer months (not shown; 775 radar–gauge pairs), i.e., an extension of Fig. 6: the relative bias improves from  $-46\%$  to  $-36\%$  and the Pearson correlation coefficient increases from 0.72 to 0.77, which is comparable to Figueras i Ventura et al. (2012).



Jacobi and Heistermann (2016) evaluate hourly rainfall for the MK method for different rain gauge thresholds, where hourly time intervals in which none of the gauges exceeded a minimum threshold were discarded. They use data from one radar in southwest Germany. Although it is at a similar latitude as the Netherlands, differences in climate exist, notably caused by orography. Their results for a threshold of 1 mm can be compared to those for the MK method in Fig. 6. Note that the thresholding in Fig. 6 is applied to individual radar–gauge pairs instead of entire time intervals, which hampers an exact comparison. Their underestimation decreases from  $-51.6\%$  without attenuation correction to  $-43.6\%$  for the MK method. In Fig. 6 the underestimation decreases from  $-52.2\%$  without attenuation correction to  $-47.4\%$  for the MK method. In the current study, only the Kdp method gives a similar improvement ( $-43.7\%$ ).

## 6. Conclusions

An intercomparison of a single-pol and a dual-pol attenuation correction method was presented, evaluating a 318-day dataset of two C-band radars in a temperate climate to correct for rain-induced attenuation: 1) modified Kraemer based on Hirschfeld–Bordan where parameters of the power-law  $k_h$ – $Z_h$  relation were adjusted such that reflectivities in the entire dataset do not exceed 59 dBZ<sub>h</sub> and attenuation correction was limited to 10 dB (MK method); 2) two-way path-integrated attenuation (PIA) computed from specific differential phase (Kdp method). Only radar voxels with echoes classified as meteorological and below the freezing-level height contributed to the computation of PIA. This was achieved by employing the forecasted freezing-level height from the numerical weather prediction model HARMONIE-AROME. An extensive evaluation with rain gauge data showed that both attenuation correction methods generally improve QPE, mainly by yielding a lower underestimation, where the improvement is strong for rainfall extremes. The Kdp method provided clearly better results than the MK method. The verification especially revealed that the underestimation reduces from 51% to 44% for daily radar–gauge pairs (gauge rainfall >1 mm) for the Kdp method. Moreover, that the underestimation diminishes from 55% to 37% for hourly rainfall for the Kdp method when the radar and/or gauge indicates more than 10 mm of rain in that hour. The improvement for the MK method was less pronounced, with a resulting underestimation of 48% (daily) and 40% (hourly).

The average improvement of the relative bias in rainfall accumulations for the Kdp method also gives an indication of the effect of attenuation on QPE. Attenuation by rainfall accounts for approximately 7% underestimation in the Netherlands over all seasons and intensities. This contribution rises to approximately 18% for hourly rainfall depths above 10 mm. The relative importance of attenuation will be different in other climates and for different wavelengths.

The long-term evaluation gives confidence that both methods can be reliably applied in an operational setting. The stability of the MK method holds a promise for application to climatological data archives from single-pol radars. Apparently, this Hirschfeld and Bordan type of algorithm is stable due to its

constraints, which is consistent with Jacobi and Heistermann (2016). Moreover, we encourage other researchers to evaluate our and other (e.g., Testud et al. 2000; Bringi et al. 2001; Gu et al. 2011; Vulpiani et al. 2012; Gou et al. 2019) Kdp-based attenuation correction methods on long radar datasets, from other radars and in other climates. For instance, Tabary et al. (2011) compare Kdp-based attenuation correction methods for 12 events in France, captured by a C-band radar, finding a better performance for the ZPHI method compared to the basic method (Bringi et al. 1990), which is also employed in our study.

We have also provided a method to estimate uncertainties in attenuation-corrected  $Z_h$  based on the variability of raindrop size distributions. This quality information can be used for merging data from different radars, but also for generating uncertainty estimates in radar QPE products. These uncertainties can be very useful for many applications of QPE, such as hydrological modeling.

The open-source wradlib attenuation correction methods were applied. Freely available and well-documented libraries help to start research on improving QPE more easily. In addition, it facilitates reproduction of findings as in this study and has potential for implementation in operational processing chains.

Finally, this study reveals that the KNMI radars still underestimate rainfall with respect to rain gauge data, where the underestimation is especially strong in winter. The large systematic underestimations could be remedied to some extent by applying a default bias correction based on historical comparisons with rain gauge data. However, we advocate to first improve the radar data applying physically based methods and then adjust radar data using rain gauge data from the same time intervals. This shows the need for follow-up studies to improve QPE. For instance, through application of vertical profile of reflectivity correction algorithms (Hazenbergh et al. 2013) or through polarimetry, e.g., by computing rainfall intensities from specific differential phase in case of moderate to heavy rainfall. Also attenuation due to other precipitation types, e.g., in melting hail (Ryzhkov et al. 2013), and especially melting snow in the bright band could be investigated and corrected for, although this is expected to play a minor role for the Netherlands. Instead, developing a correction for attenuation due to wet radomes (e.g., van de Beek et al. 2016) is considered more important for QPE and other applications.

*Acknowledgments.* We gratefully acknowledge funding from “Slim Water Management” program administered by Rijkswaterstaat on behalf of the Dutch Ministry of Infrastructure and Water Management, from the Foundation for Applied Water Research STOWA, and from “het Waterschapshuis,” representing the 21 Dutch water boards, for the project “Onderzoek neerslagmetingen.” We thank the three anonymous reviewers for their constructive comments.

*Data availability statement.* The data employed in this study are freely available. The volumetric radar data can be retrieved from the KNMI Data Platform (<https://dataplatfom.knmi.nl/dataset/radar-tar-volume-denhelder-1-0> and <https://dataplatfom.knmi.nl/dataset/radar-tar-vol-full-herwijnen-1-0>), as well as the interpolated

manual rain gauge data (<https://dataplatfom.knmi.nl/dataset/rdl-5>). The automatic and manual rain gauge data are provided by KNMI (<https://www.knmi.nl/nederland-nu/klimatologie/uurgegevens> and <https://www.knmi.nl/nederland-nu/klimatologie/monv/reeksen>; websites are in Dutch). The dataset of forecasted freezing-level height from the numerical weather prediction model HARMONIE-AROME is available from the 4TU. Centre for Research Data: <https://doi.org/10.4121/uuid:b5ad2400-e7b3-43f8-8b82-ddde877ff3ee>.

## REFERENCES

- Al-Sakka, H., A.-A. Boumahmoud, B. Fradon, S. J. Frasier, and P. Tabary, 2013: A new fuzzy logic hydrometeor classification scheme applied to the French X-, C-, and S-band polarimetric radars. *J. Appl. Meteor. Climatol.*, **52**, 2328–2344, <https://doi.org/10.1175/JAMC-D-12-0236.1>.
- Andsager, K., K. V. Beard, and N. F. Laird, 1999: Laboratory measurements of axis ratios for large raindrops. *J. Atmos. Sci.*, **56**, 2673–2683, [https://doi.org/10.1175/1520-0469\(1999\)056<2673:LMOARF>2.0.CO;2](https://doi.org/10.1175/1520-0469(1999)056<2673:LMOARF>2.0.CO;2).
- Beard, K. V., 1976: Terminal velocity and shape of cloud and precipitation drops aloft. *J. Atmos. Sci.*, **33**, 851–864, [https://doi.org/10.1175/1520-0469\(1976\)033<0851:TVASOC>2.0.CO;2](https://doi.org/10.1175/1520-0469(1976)033<0851:TVASOC>2.0.CO;2).
- Beekhuis, H., and T. Mathijssen, 2018: From pulse to product, highlights of the upgrade project of the Dutch national weather radar network. *10th European Conf. on Radar in Meteorology and Hydrology*, Wageningen, Netherlands, Wageningen University and Research, 960–965, <https://doi.org/10.18174/454537>.
- Bengtsson, L., and Coauthors, 2017: The HARMONIE-AROME model configuration in the ALADIN-HIRLAM NWP system. *Mon. Wea. Rev.*, **145**, 1919–1935, <https://doi.org/10.1175/MWR-D-16-0417.1>.
- Bringi, V. N., and V. Chandrasekar, 2001: *Polarimetric Doppler Weather Radar: Principles and Applications*. Cambridge University Press, 636 pp.
- , —, N. Balakrishnan, and D. S. Zrnić, 1990: An examination of propagation effects in rainfall on radar measurements at microwave frequencies. *J. Atmos. Oceanic Technol.*, **7**, 829–840, [https://doi.org/10.1175/1520-0426\(1990\)007<0829:AEPEPI>2.0.CO;2](https://doi.org/10.1175/1520-0426(1990)007<0829:AEPEPI>2.0.CO;2).
- , T. D. Keenan, and V. Chandrasekar, 2001: Correcting C-band radar reflectivity and differential reflectivity data for rain attenuation: A self-consistent method with constraints. *IEEE Trans. Geosci. Remote Sens.*, **39**, 1906–1915, <https://doi.org/10.1109/36.951081>.
- Carey, L. D., S. A. Rutledge, D. A. Ahijevych, and T. D. Keenan, 2000: Correcting propagation effects in C-band polarimetric radar observations of tropical convection using differential propagation phase. *J. Appl. Meteor.*, **39**, 1405–1433, [https://doi.org/10.1175/1520-0450\(2000\)039<1405:CPEICB>2.0.CO;2](https://doi.org/10.1175/1520-0450(2000)039<1405:CPEICB>2.0.CO;2).
- Crisologo, I., G. Vulpiani, C. C. Abon, C. P. C. David, A. Bronstert, and M. Heistermann, 2014: Polarimetric rainfall retrieval from a C-band weather radar in a tropical environment (the Philippines). *Asia-Pac. J. Atmos. Sci.*, **50**, 43–55, <https://doi.org/10.1007/s13143-014-0049-y>.
- de Haan, S., and A. Stoffelen, 2012: Assimilation of high-resolution Mode-S wind and temperature observations in a regional NWP model for nowcasting applications. *Wea. Forecasting*, **27**, 918–937, <https://doi.org/10.1175/WAF-D-11-00088.1>.
- Diederich, M., A. Ryzhkov, C. Simmer, P. Zhang, and S. Trömel, 2015: Use of specific attenuation for rainfall measurement at X-band radar wavelengths. Part II: Rainfall estimates and comparison with rain gauges. *J. Hydrometeorol.*, **16**, 503–516, <https://doi.org/10.1175/JHM-D-14-0067.1>.
- Dolan, B., S. A. Rutledge, S. Lim, V. Chandrasekar, and M. Thurai, 2013: A robust C-band hydrometeor identification algorithm and application to a long-term polarimetric radar dataset. *J. Appl. Meteor. Climatol.*, **52**, 2162–2186, <https://doi.org/10.1175/JAMC-D-12-0275.1>.
- Fabry, F., 2015: *Radar Meteorology: Principles and Practice*. Cambridge University Press, 256 pp., <https://doi.org/10.1017/CBO9781107707405>.
- Figueras i Ventura, J., A.-A. Boumahmoud, B. Fradon, P. Dupuy, and P. Tabary, 2012: Long-term monitoring of French polarimetric radar data quality and evaluation of several polarimetric quantitative precipitation estimators in ideal conditions for operational implementation at C-band. *Quart. J. Roy. Meteor. Soc.*, **138**, 2212–2228, <https://doi.org/10.1002/qj.1934>.
- Gou, Y., H. Chen, and J. Zheng, 2019: An improved self-consistent approach to attenuation correction for C-band polarimetric radar measurements and its impact on quantitative precipitation estimation. *Atmos. Res.*, **226**, 32–48, <https://doi.org/10.1016/j.atmosres.2019.03.006>.
- Gu, J.-Y., A. Ryzhkov, P. Zhang, P. Neilley, M. Knight, B. Wolf, and D.-I. Lee, 2011: Polarimetric attenuation correction in heavy rain at C band. *J. Appl. Meteor. Climatol.*, **50**, 39–58, <https://doi.org/10.1175/2010JAMC2258.1>.
- Hazenberg, P., H. Leijnse, and R. Uijlenhoet, 2011: Radar rainfall estimation of stratiform winter precipitation in the Belgian Ardennes. *Water Resour. Res.*, **47**, W02507, <https://doi.org/10.1029/2010WR009068>.
- , P. J. J. F. Torfs, H. Leijnse, G. Delrieu, and R. Uijlenhoet, 2013: Identification and uncertainty estimation of vertical reflectivity profiles using a Lagrangian approach to support quantitative precipitation measurements by weather radar. *J. Geophys. Res. Atmos.*, **118**, 10 243–10 261, <https://doi.org/10.1002/jgrd.50726>.
- Heistermann, M., S. Jacobi, and T. Pfaff, 2013: Technical Note: An open source library for processing weather radar data (wraddlib). *Hydrol. Earth Syst. Sci.*, **17**, 863–871, <https://doi.org/10.5194/hess-17-863-2013>.
- Hitschfeld, W., and J. Bordan, 1954: Errors inherent in the radar measurement of rainfall at attenuating wavelengths. *J. Meteorol.*, **11**, 58–67, [https://doi.org/10.1175/1520-0469\(1954\)011<0058:EIITRM>2.0.CO;2](https://doi.org/10.1175/1520-0469(1954)011<0058:EIITRM>2.0.CO;2).
- Holleman, I., 2006: Bias adjustment of radar-based 3-hour precipitation accumulations. KNMI Tech. Rep. TR-290, 56 pp., [https://cdn.knmi.nl/system/data\\_center\\_publications/files/000/067/347/original/tr\\_3houraccu.pdf?1495620726](https://cdn.knmi.nl/system/data_center_publications/files/000/067/347/original/tr_3houraccu.pdf?1495620726).
- , 2007: Bias adjustment and long-term verification of radar-based precipitation estimates. *Meteor. Appl.*, **14**, 195–203, <https://doi.org/10.1002/met.22>.
- Hong, Y., and J. Gourley, 2015: *Radar Hydrology: Principles, Models, and Applications*. CRC Press, 176 pp., <https://doi.org/10.1201/b17921>.
- Hubbert, J., and V. N. Bringi, 1995: An iterative filtering technique for the analysis of copolar differential phase and dual-frequency radar measurements. *J. Atmos. Oceanic Technol.*, **12**, 643–648, [https://doi.org/10.1175/1520-0426\(1995\)012<0643:AIFTFT>2.0.CO;2](https://doi.org/10.1175/1520-0426(1995)012<0643:AIFTFT>2.0.CO;2).
- Jacobi, S., and M. Heistermann, 2016: Benchmarking attenuation correction procedures for six years of single-polarized C-band weather radar observations in south-west Germany. *Geomatics Nat. Hazards Risk*, **7**, 1785–1799, <https://doi.org/10.1080/19475705.2016.1155080>.

- Jaffrain, J., and A. Berne, 2011: Experimental quantification of the sampling uncertainty associated with measurements from Parsivel disdrometers. *J. Hydrometeorol.*, **12**, 352–370, <https://doi.org/10.1175/2010JHM1244.1>.
- KNMI, 2000: Handbook for the meteorological observation. KNMI Doc., 112 pp., <https://www.knmi.nl/projects/documents/publications/2006/01/01/handbook-for-the-meteorological-observation>.
- Leijnse, H., and Coauthors, 2010: Precipitation measurement at CESAR, the Netherlands. *J. Hydrometeorol.*, **11**, 1322–1329, <https://doi.org/10.1175/2010JHM1245.1>.
- , H. Beekhuis, and I. Holleman, 2016: Doppler clutter removal on KNMI weather radars. KNMI Tech. Rep. TR-355, 40 pp., <http://publicaties.minienm.nl/download-bijlage/80785/doppler-clutter-removal-on-knmi-weather-radars.pdf>.
- Liebe, H. J., G. A. Hufford, and T. Manabe, 1991: A model for the complex permittivity of water at frequencies below 1 THz. *Int. J. Infrared Millimeter Waves*, **12**, 659–675, <https://doi.org/10.1007/BF01008897>.
- Marra, F., and E. Morin, 2015: Use of radar QPE for the derivation of intensity–duration–frequency curves in a range of climatic regimes. *J. Hydrol.*, **531**, 427–440, <https://doi.org/10.1016/j.jhydrol.2015.08.064>.
- Marshall, J. S., W. Hirschfeld, and K. L. S. Gunn, 1955: Advances in radar weather. *Advances in Geophysics*, Vol. 2, Academic Press, 1–56, [https://doi.org/10.1016/S0065-2687\(08\)60310-6](https://doi.org/10.1016/S0065-2687(08)60310-6).
- Mishchenko, M. I., 2000: Calculation of the amplitude matrix for a nonspherical particle in a fixed orientation. *Appl. Opt.*, **39**, 1026–1031, <https://doi.org/10.1364/AO.39.001026>.
- Mühlbauer, K., and M. Heistermann, 2019: wradlib/wradlib: wradlib release 1.4.2. Zenodo, <https://doi.org/10.5281/zenodo.3245745>.
- Overeem, A., I. Holleman, and A. Buishand, 2009: Derivation of a 10-year radar-based climatology of rainfall. *J. Appl. Meteor. Climatol.*, **48**, 1448–1463, <https://doi.org/10.1175/2009JAMC1954.1>.
- , R. Uijlenhoet, and H. Leijnse, 2020: Full-year evaluation of nonmeteorological echo removal with dual-polarization fuzzy logic for two C-band radars in a temperate climate. *J. Atmos. Oceanic Technol.*, **37**, 1643–1660, <https://doi.org/10.1175/JTECH-D-19-0149.1>.
- Rauber, R. M., and S. L. Nesbitt, 2018: *Radar Meteorology: A First Course*. John Wiley and Sons, 488 pp., <https://www.wiley.com/en-us/Radar+Meteorology%3A+A+First+Course-p-9781118432624>.
- Ryzhkov, A., and D. S. Zrnić, 1995: Precipitation and attenuation measurements at a 10-cm wavelength. *J. Appl. Meteor.*, **34**, 2121–2134, [https://doi.org/10.1175/1520-0450\(1995\)034<2120:PAAMAA>2.0.CO;2](https://doi.org/10.1175/1520-0450(1995)034<2120:PAAMAA>2.0.CO;2).
- , and —, 2019: *Radar Polarimetry for Weather Observations*. Springer, 486 pp., <https://doi.org/10.1007/978-3-030-05093-1>.
- , P. Zhang, D. Hudak, J. Alford, M. Knight, and J. Conway, 2007: Validation of polarimetric methods for attenuation correction at C band. *33rd Conf. on Radar Meteorology*, Cairns, Australia, Amer. Meteor. Soc., P11B.12, <http://ams.confex.com/ams/pdfpapers/123122.pdf>.
- , M. R. Kumjian, S. M. Ganson, and P. Zhang, 2013: Polarimetric radar characteristics of melting hail. Part II: Practical implications. *J. Appl. Meteor. Climatol.*, **52**, 2871–2886, <https://doi.org/10.1175/JAMC-D-13-074.1>.
- , M. Diederich, P. Zhang, and C. Simmer, 2014: Potential utilization of specific attenuation for rainfall estimation, mitigation of partial beam blockage, and radar networking. *J. Atmos. Oceanic Technol.*, **31**, 599–619, <https://doi.org/10.1175/JTECH-D-13-00038.1>.
- Tabary, P., G. Vulpiani, J. J. Gourley, A. J. Illingworth, R. J. Thompson, and O. Bousquet, 2009: Unusually high differential attenuation at C band: Results from a two-year analysis of the French Trappes polarimetric radar data. *J. Appl. Meteor. Climatol.*, **48**, 2037–2053, <https://doi.org/10.1175/2009JAMC2039.1>.
- , A.-A. Boumahmoud, H. Andrieu, R. J. Thompson, A. J. Illingworth, E. L. Bouar, and J. Testud, 2011: Evaluation of two “integrated” polarimetric quantitative precipitation estimation (QPE) algorithms at C-band. *J. Hydrol.*, **405**, 248–260, <https://doi.org/10.1016/j.jhydrol.2011.05.021>.
- Testud, J., E. Le Bouar, E. Obligis, and M. Ali-Mehenni, 2000: The rain profiling algorithm applied to polarimetric weather radar. *J. Atmos. Oceanic Technol.*, **17**, 332–356, [https://doi.org/10.1175/1520-0426\(2000\)017<0332:TRPAAT>2.0.CO;2](https://doi.org/10.1175/1520-0426(2000)017<0332:TRPAAT>2.0.CO;2).
- Thorndahl, S., J. E. Nielsen, and M. R. Rasmussen, 2014: Bias adjustment and advection interpolation of long-term high resolution radar rainfall series. *J. Hydrol.*, **508**, 214–226, <https://doi.org/10.1016/j.jhydrol.2013.10.056>.
- Tokay, A., D. B. Wolff, and W. A. Petersen, 2014: Evaluation of the new version of the laser-optical disdrometer, OTT Parsivel<sup>2</sup>. *J. Atmos. Oceanic Technol.*, **31**, 1276–1288, <https://doi.org/10.1175/JTECH-D-13-00174.1>.
- Trömel, S., M. Ziegert, A. V. Ryzhkov, C. Chwala, and C. Simmer, 2014: Using microwave backhaul links to optimize the performance of algorithms for rainfall estimation and attenuation correction. *J. Atmos. Oceanic Technol.*, **31**, 1748–1760, <https://doi.org/10.1175/JTECH-D-14-00016.1>.
- van de Beek, C. Z., H. Leijnse, J. N. M. Stricker, R. Uijlenhoet, and H. W. J. Russchenberg, 2010: Performance of high-resolution X-band radar for rainfall measurement in the Netherlands. *Hydrol. Earth Syst. Sci.*, **14**, 205–221, <https://doi.org/10.5194/hess-14-205-2010>.
- , —, P. Hazenberg, and R. Uijlenhoet, 2016: Close-range radar rainfall estimation and error analysis. *Atmos. Meas. Tech.*, **9**, 3837–3850, <https://doi.org/10.5194/amt-9-3837-2016>.
- Vulpiani, G., P. Tabary, J. Parent du Chatelet, and F. S. Marzano, 2008: Comparison of advanced radar polarimetric techniques for operational attenuation correction at C band. *J. Atmos. Oceanic Technol.*, **25**, 1118–1135, <https://doi.org/10.1175/2007JTECHA936.1>.
- , M. Montopoli, L. D. Passeri, A. G. Gioia, P. Giordano, and F. S. Marzano, 2012: On the use of dual-polarized C-band radar for operational rainfall retrieval in mountainous areas. *J. Appl. Meteor. Climatol.*, **51**, 405–425, <https://doi.org/10.1175/JAMC-D-10-05024.1>.
- Wessels, H. R. A., 1972: Metingen van regendruppels te De Bilt (in Dutch). KNMI Scientific Rep. WR 72-6, 46 pp., <http://publicaties.minienm.nl/download-bijlage/7976/metingen-van-regendruppels-te-de-bilt.pdf>.
- wradlib, 2020: wradlib.atten.correct\_attenuation\_constrained. wradlib, [https://docs.wradlib.org/en/stable/generated/wradlib.atten.correct\\_attenuation\\_constrained.html](https://docs.wradlib.org/en/stable/generated/wradlib.atten.correct_attenuation_constrained.html).
- Zhang, G., 2017: *Weather Radar Polarimetry*. CRC Press, 304 pp.